Dynamics of the Canadian Arctic Archipelago throughflow: A numerical study with a finite element sea ice and ocean model

Claudia Wekerle

Universität Bremen, 2013

Universität Bremen

ALFRED-WEGENER-INSTITUT
HELMHOLTZ-ZENTRUM FÜR POLAR-
UND MEERESFORSCHUNG

Dynamics of the Canadian Arctic Archipelago throughflow: A numerical study with a finite element sea ice and ocean model

Von der Fakultät für Physik und Elektrotechnik
der Universität Bremen
zur Erlangung des akademischen Grades
einer **Doktorin der Naturwissenschaften (Dr. rer. nat.)**
genehmigte Dissertation

von

Claudia Wekerle

Gutachter: Prof. Dr. Peter Lemke

Zweitgutachter: Prof. Dr. Thomas Jung

Eingereicht am 4. Juni 2013

Tag des Promotionskolloquiums: 13. September 2013

Declaration of Authorship

I certify that the work presented here is, to the best of my knowledge and belief, original and the result of my own investigations, except as acknowledged, and has not been submitted, either in part or whole, for a degree at this or any other University.

Bremerhaven, June 2013

Abstract

The Canadian Arctic Archipelago (CAA) connects the Arctic Ocean and Baffin Bay through narrow channels and is one of the key gateways where freshwater leaves the Arctic. It has therefore the potential to affect the deep convection in the northern North Atlantic.

Representing the CAA in traditional global models still poses a challenge due to the small scale nature of the narrow passages. In this study we apply a global, multi-resolution sea ice ocean model (the Finite Element Sea ice Ocean Model, FESOM) with refinement in the CAA up to ∼5 km while keeping a coarse resolution setup otherwise. With this model setup, a hindcast simulation for the period 1968-2007 was performed.

The first goal of this thesis is to assess the model behavior in the CAA region and in the Arctic Ocean. The model assessment revealed good agreement with sea ice conditions in the Arctic Ocean and with fluxes through the main gates of the Arctic Ocean. During the period 1968-2007 the mean volume transports through Lancaster Sound and Nares Strait amount to 0.86 Sv (1 Sv = 10^6 m³/s) and 0.91 Sv, respectively. The monthly mean volume transport through western Lancaster Sound is highly correlated with the observational estimate (r=0.81). A comparison of simulated sectionally averaged velocities in Nares Strait with observational estimates reveals good agreement (r=0.57). The simulated mean CAA freshwater export rate is 123 mSv, slightly higher than the observational estimate (101±10 mSv). The local refinement of ∼5 km allows to investigate the freshwater contribution of individual narrow straits to the Parry Channel.

In the second part of the thesis, the mechanisms driving the interannual variability of freshwater transports through the CAA are analyzed. The

interannual variability is determined by sea surface height (SSH) gradients between the Arctic Ocean and northern Baffin Bay. The variability of fluxes through Lancaster Sound and Nares Strait is mainly determined by that of the SSH on the shelf along the Beaufort Sea coast and in the northeastern Baffin Bay, respectively. Sea level variations north of the CAA are explained by changes in the wind regimes (cyclonic vs. anticyclonic) associated to release or accumulation of freshwater from the Beaufort Gyre, whereas sea level in the northeastern Baffin Bay can be attributed to ocean-atmosphere heat fluxes over the Labrador Sea. Both processes are linked with the North Atlantic Oscillation type of atmospheric variability.

In the last part of the thesis, the effect of mesh resolution in the CAA area is evaluated by performing experiments with and without highly resolved archipelago ($\sim$5 km vs. $\sim$24 km resolution). Increased resolution in the CAA leads to higher freshwater transports through the CAA; at the same time transports on the eastern side of Greenland are reduced. The 'redirection' of Arctic freshwater affects convection in the Labrador Sea and thus the Atlantic meridional overturning circulation.

We conclude that multi-resolution models like FESOM are promising tools for global climate modeling, as they are able to present small scale processes in a global setup.

Zusammenfassung

Das Kanadisch-Arktische Archipel (CAA) verbindet den Arktischen Ozean mit der Baffin-Bucht und ist eines der Hauptausgänge durch welches süßere Arktische Wassermassen in den salzhaltigeren Nordatlantik fließen. Das Süßwasser arktischen Ursprungs hat das Potenzial, die Tiefenwasserbildung im Nordatlantik zu beeinflussen.

Aufgrund der engen Wasserstraßen ist es nicht möglich, das kanadische Archipel in traditionellen globalen Ozeanmodellen adequat zu repräsentieren. In dieser Arbeit wird das Finite Elemente Meereis Ozean Modell (FESOM) verwendet, um die Ozean- und Meereisdynamik des Archipels zu simulieren. Der Vorteil von FESOM liegt in der Finite-Elemente Diskretisierung, welche die Verwendung von unstrukturierten Gittern ermöglicht. Dadurch kann das kanadische Archipel hoch aufgelöst werden (in dieser Modellversion bis ~ 5 km), während andere Teile der Weltozeane gröber aufgelöst werden können.

Das erste Ziel dieser Arbeit ist die Validierung des Modells anhand von Beobachungen im Kanadischen Archipel und im Arktischen Ozean. Die Modellergebnisse zeigen gute Übereinstimmung mit den Meereisbedingungen im Arktischen Ozean und mit gemessenen Volumen- und Süßwassertransporten durch die Ausfallstore des Arktischen Ozeans (Beringstraße, Davisstraße, Framstraße und Barentssee). Während der Zeitperiode 1968-2007 beträgt der simulierte mittlere Volumentransport durch den Lancastersund 0.86 Sv (1 Sv = 10^6 m³/s), während der Transport durch die Naresstraße 0.91 Sv beträgt. Der monatliche simulierte Volumentransport durch den westlichen Lancastersund ist mit Beobachtungsdaten signifikant korreliert (r=0.81). Ein Vergleich von simulierten mittleren Geschwindigkeiten in der Naresstraße mit beobachteten Geschwindigkeiten zeigt gute Übereinstimmung

(r=0.57). Der mittlere simulierte Süßwasserexport des kanadischen Archipels beträgt 123 mSv, und ist etwas höher als der Beobachtungswert (101±10 mSv). Durch die lokale Gitterverfeinerung von ∼5 km lässt sich der Süßwassereinfluss durch die einzelnen engen Passagen in den Parry-Kanal analysieren.

Im zweiten Teil dieser Arbeit werden die Kontrollmechanismen der zwischenjährlichen Variabilität der Süßwassertransporte durch das CAA untersucht. Die zwischenjährliche Variabilität wird durch den Meeresspiegelgradienten zwischen dem Arktischen Ozean und der nördlichen Baffin-Bucht bestimmt. Die Variabilität der Transporte durch den Lancastersund wird hauptsächlich durch den Meeresspiegel entlang der Beaufortsee bestimmt, während der Süßwassertransport durch die Naresstraße durch den Meeresspiegel in der nordöstlichen Baffin-Bucht bestimmt wird. Meeresspiegeländerungen nördlich des kanadischen Archipels können duch Änderungen im Windregime (zyklonisch vs. antizyklonisch) erklärt werden, welche mit einer Akkumulation oder Freigabe von Süßwasser im Beaufortwirbel verbunden sind. Meeresspiegeländerungen in der nordöstlichen Baffin-Bucht dagegen können mit Wärmeflüßen zwischen Ozean und Atmosphäre in der Labradorsee erklärt werden. Beide Prozesse sind an die atmosphärische Variabilität der Nordatlantischen Oszillation gekoppelt.

Im letzten Teil dieser Arbeit wird der Effekt der Gitterauflösung im Bereich des Kanadischen Archipels untersucht, indem Experimente mit und ohne hoch aufgelöstes Archipel durchgeführt wurden (∼5 km vs. ∼24 km Auflösung). Hohe Auflösung im CAA führt zu höheren Süßwassertransporten durch das CAA; gleichzeitig sinken die Transporte östlich von Grönland. Durch diese 'Umleitung' des Arktichen Süßwassers ändert sich die Tiefenwasserbildung in der Labradorsee, und damit auch die Atlantische meridionale Umwälzzirkulation.

Zusammenfassend lässt sich sagen, dass multi-skalen Modelle wie FESOM im Vergleich zu tradionellen Ozeanmodellen Vorteile bieten: So können etwa in einer globalen Konfiguration klein-skalige Prozesse modelliert werden, während eine bessere Darstellung der klein-skaligen Prozesse zu einer besseren Darstellung der groß-skaligen Zirkulation führt.

Contents

Chapter 1

Introduction

1.1 The Canadian Arctic Archipelago - Background

The Arctic Ocean, enclosed by American and Eurasian landmasses and Greenland, has only limited connections to the world oceans. The stratification of water masses in the Arctic Ocean is strongly influenced by the presence of fresh surface waters originating from high river runoff through Siberian and North American rivers, precipitation in form of snow and low evaporation due to the isolating ice cover, and inflow of less saline Pacific Water through Bering Strait (*Serreze et al.*, 2006; *Dickson et al.*, 2007). These relatively fresh waters exit mainly through two passages: Fram Strait and the Canadian Arctic Archipelago (CAA).

While Fram Strait is a deep (sill depth 2,600 m) and broad passway, the CAA is a shallow shelf system with narrow straits, characterized by a complex bathymetry. Water and sea ice exiting the CAA have to pass through one of the four exits: Lancaster Sound, Smith Sound or Jones Sound to Baffin Bay, or Fury and Hecla Strait to Foxe Basin (see Figure 1.1). Parry Channel, which opens out at its eastern end into Lancaster Sound, is the largest strait of the CAA and has a width of 52.3 km at its narrowest point. Nares Strait, the CAA's easternmost strait which ends in Smith Sound in the south, has a minimum width of 27.7 km.

Figure 1.1: Model bathymetry of the Canadian Arctic Archipelago.

Table 1.1: Abbreviations used in Figure 1.1.

AG	Amundsen Gulf	LS	Lancaster Sound
BaI	Banks Island	MCC	McClintock Channel
BI	Baffin Island	MCS	McClure Strait
BMC	Byam Martin Channel	MI	Melville Island
BS	Barrow Strait	PeS	Penny Strait
DI	Devon Island	PRI	Prince Regent Inlet
EI	Ellesmere Island	PS	Peel Sound
GL	Greenland	PWI	Prince of Wales Island
FHS	Fury and Hecla Strait	PWS	Prince of Wales Strait
HC	Hell Gate/Cardigan Strait	QEI	Queen Elizabeth Islands
JS	Jones Sound	RC	Robeson Channel
KC	Kennedy Channel	SS	Smith Sound
KWI	King William Island	VI	Victoria Island

Hell Gate and Cardigan Strait open out into Jones Sound and have a minimum total width of 12.4 km (see *Melling* (2000) for more details). Fury and Hecla Strait is 2 km wide. The CAA is a shelf basin with sills ranging from 125 m in western Lancaster Sound and Hell Gate to 220 m in Nares Strait (*Melling*, 2000). The shallow sills retain salty Arctic Ocean waters originating from the North Atlantic and permit fresh surface water to flow southwards.

Despite the potential importance of the CAA region in the climate system, in situ measurements of the ocean hydrography and velocity in this region are still rather sparse in time and space due to its remote location and harsh weather conditions. The circulation in the Canadian Arctic Archipelago is generally considered to be directed from the Arctic Ocean towards the south east (*Walker*, 1977). Based on data from the cruise of *HMCS Labrador* in 1954[1] from Baffin Bay through Parry Channel, Prince of Wales Strait to the Beaufort Sea, *Bailey* (1957) was one of the first to give a detailed description of the density structure of the water masses along the North West Passage (NWP), a sea route between the Atlantic and Pacific oceans passing through the Canadian archipelago. He described that Arctic waters enter Parry Channel, the northern most part of the North West Passage, mainly through McClure Strait, Byam Martin Channel and Penny Strait.

The flow through Parry Channel bifurcates at around 102°W, where parts of the water flows southwards through McClintock Channel and then enters Parry Channel again through Peel Sound (*Wang et al.*, 2012a). Mooring measurements in Peel Sound in April 1981 revealed a northward transport of 0.17 Sv, which equals one-third of the eastward transport in Barrow Strait (*Prinsenberg and Bennet*, 1989).

Long term oceanographic measurements were carried out primarily in Barrow Strait (western Lancaster Sound) for the period of 1998-2011 (*Prinsenberg et al.*, 2009; *Peterson et al.*, 2012): Volume and freshwater transport exhibits a strong seasonal variability, with peaks in summer and small fluxes in fall and early winter. Apart from the strong eastward current which dom-

---

[1]The first large vessel to circumnavigate North America through the North West Passage from east to west in a single year was the Canadian government icebreaker Labrador.

inates the central and southern part of the Lancaster Sound cross section, observations indicated a weak westward counter current on the northern side appearing particularly in the summer months. *Peterson et al.* (2012) found a significant correlation of transport through this strait with northeastward wind anomalies in the Beaufort Sea, indicating that a cyclonic wind pattern over the Beaufort Sea would favor high transports through Lancaster Sound.

Mooring measurements in Cardigan Strait and Hell Gate were performed from 1998 on (*Melling et al.*, 2008), estimating volume fluxes of 0.2 Sv and 0.1 Sv, respectively (for the 1998-2002 time period). There is an indication that the strongest Arctic outflow occurs from January through September, with weaker and even reversing flows in autumn and early winter.

Moorings deployed from 2003-2006 indicated that the flow through Nares Strait is mainly directed from north to south, with a small counter current accounting for around 5% of the southward flow (*Münchow and Melling*, 2008). For this time period, the mean volume transport was estimated as 0.57±0.09 Sv (excluding the top 30 m).

The main oceanic feature in eastern Lancaster Sound and western Baffin Bay is the Baffin Island Current, which receives water mass contributions from Smith, Jones and Lancaster Sounds, as well as from the West Greenland Current, and continues southwards along the western side of Baffin Bay. *Fissel et al.* (1982), based on observations in the summers of 1978 and 1979, observed the Baffin Island Current to penetrate westwards into Lancaster Sound for 35 to 75 km along its northern side, before crossing to the southern side and exiting to the east. In the mouth of Lancaster Sound, they observed surface speeds up to 75 cm/s, and an average width of the flow of 10 to 30 km.

The CAA is covered by sea ice most of the year, with some regions in the south and east opening up in late summer. September is generally the month with the lowest sea ice concentration. Freezing starts again in October, and the sea ice is landfast for around half a year (*Melling*, 2002). Thick multi-year ice persists along the northern boundary of the CAA, being in fact the thickest sea ice that can be found in the Arctic Ocean. The sea ice flux across the Arctic Ocean - CAA boundary was estimated by *Agnew et al.*

(2008) by evaluating AMSR-E imagery. Their study revealed an export of 77 km³ of sea ice volume each year through Amundsen Gulf and McClure Strait into the Arctic Ocean (averaged over the period 2002-2007), while Lancaster Sound exported around 102 km³ of ice volume each year into Baffin Bay. This study also showed that sea ice around the Queen Elizabeth Islands is mostly landfast. The ice drift through the narrow channels of the CAA is partly controlled by the presence of ice arches, which form especially in the northern part of Nares Strait (*Kwok*, 2005). Polynyas, fixed regions of open water that are isolated within thicker pack ice, are widely distributed over the area of the archipelago (*Hannah et al.*, 2009). Several mechanisms lead to their formation: Tides, as they mix the warmer bottom water with the colder surface waters slowing or eliminating the formation of ice, winds and currents as they drive away consolidated ice, and ice bridges (especially in Nares Strait) as they block ice upstream of the polynya area.

Climate models predict a reduction of the Arctic sea ice in the 21st century, possibly enabling a transit of the NWP for common open-water ships and moderately ice-strengthened ships during the warmest months (*Smith and Stephenson*, 2013). However, as concluded by *Wilson et al.* (2004), these projections have to be regarded with care. Increased summer air temperatures would lead to a reduction of first year ice in the region of the Queen Elizabeth Islands, allowing more multi year ice to reach the NWP through Penny Strait and Byam Martin Channel, along with a southward shift of the Beaufort Sea pack ice. The increase in drifting multi year ice in the NWP and the southward shift of pack ice present significant hazards for navigation. Additionally, the sea ice conditions in the CAA are highly variable, and occasionally there will be still summers of heavy ice conditions.

1.2   The climate relevance of the CAA

Freshwater exported from the Arctic Ocean may have a significant impact on the Atlantic Meridional Overturning Circulation (AMOC). Deep water formation (DWF) in the Labrador and Greenland Seas is initiated by a strong surface heat loss to the atmosphere, and in the Greenland Sea it is addi-

tionally activated by brine rejection from sea ice formation. This happens
particularly in the winter months. Vertical mixing leads to rising of warmer
waters and sinking of colder and more saline surface waters (*Kuhlbrodt et al.*,
2007). However, strong pulses of freshwater, as exported from the Arctic
Ocean, stabilize the density stratification in the convection areas and reduce
DWF. Deep water formed in the interior of the basins is exported by a cy-
clonic boundary current and advected southwards, and thus contributes to
the global overturning circulation (*Straneo*, 2006). It is plausible, therefore,
that an adequate representation of Arctic freshwater export in climate models
is crucial when it comes to predicting climate variability and change.

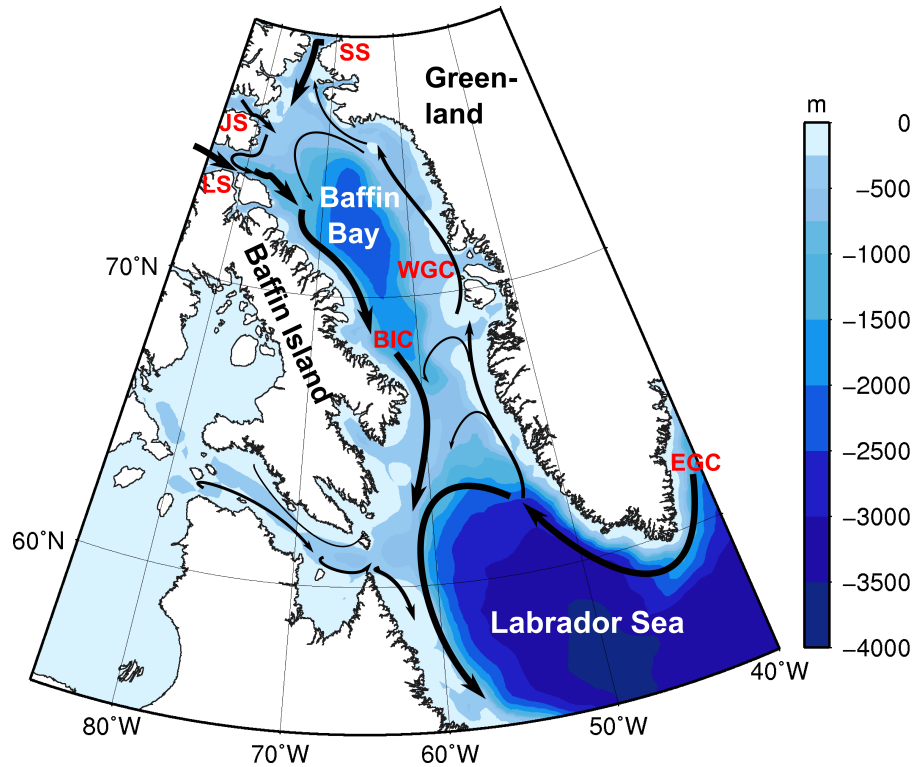Figure 1.2: Ocean circulation downstream of the CAA (LS: Lancaster Sound,
JS: Jones Sound, SS: Smith Sound, BIC: Baffin Island Current, WGC: West
Greenland Current, EGC: East Greenland Current).

Several studies were carried out to analyze the impact of freshwater ex-
ported west and east of Greenland, and came to different conclusions. *Goosse
et al.* (1997) performed experiments with a very coarse resolution sea ice-

ocean model ($3° \times 3°$ horizontal resolution), and revealed that opening the CAA passages in the model resulted in decrease of surface salinity and density in the Labrador Sea, along with a reduction of the North Atlantic Deep Water (NADW) outflow by 5%. *Wadley and Bigg* (2002) confirmed this finding: When opening the CAA passages in their model (which has a horizontal mesh resolution ranging from 100 to 800 km), the Atlantic overturning streamfunction decreased from 25 to 20 Sv. In contrast, *Komuro and Hasumi* (2005) and *Jahn et al.* (2009) came to opposite conclusions. By resolving the CAA throughflow instead of closing the CAA, both model studies showed an increase of the AMOC. The authors explained this by the redirection of freshwater pathways east and west of Greenland: If the CAA is closed, the Arctic freshwater exists mainly through Fram Strait, which is then transported via the East and West Greenland Current into the central Labrador Sea where it diminishes the convection activity. In agreement with this, *Myers* (2005) reported that enhanced freshwater export through Davis Strait has almost no impact on the Labrador Sea Water (LSW) formation since only very little of the freshwater enters the interior of the Labrador Sea (see Figure 1.2). All above studies are based on models with a rather coarse resolution.

1.3 Modeling the CAA ocean dynamics

As discussed in section 1.1, hydrographic observations are sparse in the CAA. Hence, numerical simulations can be used to reproduce the ocean circulation and to help understand the ocean dynamics in the CAA region. However, very high horizontal grid resolution is required to adequately resolve the narrow CAA straits. Because of high requirement for computational resources, numerical simulations using traditional models with high enough resolution were limited to relatively short integration time, or confined to regional model domains. Table 1.2 presents an overview of model simulations of the CAA throughflow, revealing large differences especially in the horizontal resolution. Note that all models presented in Table 1.2 are based on structured meshes. *Jahn et al.* (2012) showed that the state-of-the-art ocean models, even the regional ones, represent a large spread in the simulated CAA transport.

Table 1.2: Models simulating the CAA throughflow.

model	model domain	horizontal resolution	vertical levels	analysis period
[1]UVic ESCM	global	$1.8° \times 0.9°$	32	1950-2007
[2]ORCA025	global	10-27.75 km	46	1965-2002
[3]OCCAM	global	8.3 km	66	1989-2006
[4]NEMOv1.9/LIM2	AO/NA*	22-50 km	46	1958-2001
[5]NAME	NP/NA/AO*	$1/12°$ (~9 km)	45	1979-2004
[6]NEMOv3.1/LIM2	CAA	6.5 - 9.5 km	46	climatological forcing

[1]*Jahn et al.* (2009), [2]*Lique et al.* (2009), [3]*Aksenov et al.* (2010), [4]*Houssais and Herbaut* (2011), [5]*McGeehan and Maslowski* (2012), [6]*Wang et al.* (2012a), *NA - North Atlantic, AO - Arctic Ocean, NP - North Pacific

The geometrical complexity of the CAA suggests that exploring the role of the CAA may benefit from using models formulated on unstructured meshes. Their resolution can be conveniently refined locally with other parts of the ocean left relatively coarse. *Kliem and Greenberg* (2003) applied a regional diagnostic finite element ocean model to calculate the velocity field in the CAA based on observational data for salinity and temperature. Sea ice models using the finite element method (coupled to a slab ocean) have been used to simulate the sea ice conditions in the CAA region, and demonstrated the advantage of unstructured meshes in resolving small scale dynamics (*Lietaer et al.*, 2008; *Terwisscha van Scheltinga et al.*, 2010).

In this work numerical simulations are used to study the CAA ocean and sea ice dynamics. The simulations are performed with the Finite Element Sea-ice Ocean Model (FESOM, *Danilov et al.*, 2004; *Wang et al.*, 2008; *Timmermann et al.*, 2009), an ocean general circulation model using unstructured triangular surface meshes. Examination of its behavior on long time scales showed that FESOM performs well in simulating the past ocean variability and in representing particular climate change scenarios (*Sidorenko et al.*, 2011; *Wang et al.*, 2012b). However, these simulations used relatively coarse resolution in the CAA. Instead of refinement, the depth and width of the

CAA straits were adjusted as in most coarse-resolution models on structured meshes. In this work the model explicitly resolves the major CAA straits.

1.4 Objectives

This thesis focuses on the following questions:

- The finite element model applied in this work allows for a local refinement in areas of interest, while other parts of the world oceans can be kept relatively coarse. Taking advantage of this model feature, a new model configuration of FESOM with the CAA highly resolved within a global setup has been developed. How does this approach improve the simulation of the CAA sea ice and ocean dynamics, and does it also improve the simulation of the Arctic Ocean dynamics? In order to investigate this, we compare the model to available observations, and also to previous modeling studies.

- There is evidence that freshwater transport through the CAA has an impact on the deep water formation sites in the northern North Atlantic. Keeping this in mind, understanding the interannual variability of CAA freshwater transport is of high importance for our knowledge of the global climate. Therefore, what is the interannual variability of these transports? Which mechanisms drive the interannual variability? What is the role of atmospheric forcing in this context?

- A new high resolution modeling approach has been developed, and it is thus important to investigate the impact of mesh resolution. When resolving the CAA accurately, does this have an impact on the freshwater transports through the CAA? Does it have an impact on the convection activity in the northern North Atlantic and thus on the large scale ocean circulation? Hence, is it relevant for climate models to resolve the CAA adequately?

1.5 Contents of this thesis

The structure of this thesis is as follows. Chapter 2 describes the numerical
structure of FESOM by presenting the governing equations for the ocean and
sea ice component, their coupling, their numerical discretization based on the
finite element method, and the model setup and configuration used in this
thesis. Chapter 3 assesses the model performance in the Arctic Ocean and
in the CAA and focuses on Arctic Ocean sea ice conditions, its freshwater
budget and the CAA sea ice and ocean dynamics. The interannual variabil-
ity of freshwater transport through the CAA and its driving mechanism is
presented in Chapter 4[2]. The sensitivity to mesh resolution and impacts on
the Atlantic Ocean circulation are discussed in Chapter 5[3]. The last chapter
summarizes and discusses the main findings of this thesis.

---

[2]The major part of Chapters 3 and 4 is adopted for the following publication: Wekerle,
C., Q. Wang, S. Danilov, T. Jung and J. Schröter, Freshwater transport through the
Canadian Arctic Archipelago in a multi-resolution global model: Model assessment and
the driving mechanism of interannual variability, submitted manuscript to "Journal of
Geophysical Research", April 2013.

[3]The major part of Chapter 5 is adopted for the following publication: Wekerle, C.,
Q. Wang, S. Danilov, T. Jung, J. Schröter, and P.G. Myers, The climate relevance of
the Canadian Arctic Archipelago: A multi-resolution study, submitted manuscript to the
journal "Geophysical Research Letters", May 2013.

Chapter 2

Methods

In this work a global version of the Finite-Element-Sea ice-Ocean-Model (FE-SOM) is applied. FESOM was developed in the Climate Dynamics section of the Alfred Wegener Institute. It consists of a finite element ocean model *Danilov et al.* (2004); *Wang et al.* (2008), coupled to a sea ice model (*Timmermann et al.*, 2009). The advantage of this model is the following: The finite element discretization of the governing equations allows us to employ unstructured meshes, and therefore to locally refine the mesh in areas of interest and keep it coarse in other parts of the global oceans. This multi-resolution approach is very suitable for studying the CAA throughflow because the local fine resolution enables to resolve the complex bathymetry and narrow straits, and the global configuration avoids the open boundary and allows for studying the impact of the CAA throughflow on the global ocean circulation.

2.1   The ocean model

The ocean component solves the standard set of hydrostatic primitive equations with the Boussinesq approximation. The system of governing equations is split into two subproblems, the dynamical part and the thermodynamical part, which are solved separately.

The **dynamical** part includes the momentum equations in three dimen-

sions, the vertically integrated continuity equation and the hydrostatic pressure equation which are solved for horizontal velocity, sea surface height and pressure:

$$\partial_t \mathbf{u} + \mathbf{v} \cdot \nabla_3 \mathbf{u} + f(\mathbf{k} \times \mathbf{u}) + g\nabla\eta + \frac{1}{\rho_0}\nabla p = \nabla \cdot A_h \nabla \mathbf{u} + \partial_z A_v \partial_z \mathbf{u}, \quad (2.1)$$

$$\partial_t \eta + \nabla \cdot \int_{z=-H}^{z=\eta} \mathbf{u}\,dz = 0, \qquad\qquad (2.2)$$

$$\partial_z p = -g\,\rho, \qquad\qquad (2.3)$$

where $\mathbf{v} \equiv (\mathbf{u}, w) \equiv (u, v, v)$ is the velocity vector, $f = f(\theta)$ is the Coriolis parameter dependent on the latitude θ, $\mathbf{k}$ is the vertical unit vector, g is the gravitational acceleration, ρ_0 and ρ are the mean sea water density and the deviation from it, respectively, η is the sea surface height, $p = \int_z^0 g\,\rho\,dz$ is the hydrostatic pressure anomaly obtained by integrating the hydrostatic equation in the vertical from $z = 0$, A_h and A_v are the lateral and vertical momentum diffusion coefficients, respectively. The upper limit in the integration in equation 2.2 is set to zero, which implies a linear free-surface approximation. ∇ and ∇_3 stand for the 2-dimensional and 3-dimensional gradient and divergence operators, respectively. In equation 2.2, the transport of freshwater into and out of the ocean through the surface is omitted (transport into the ocean occurs through precipitation, river runoff and sea ice melting, while transport out of the ocean occurs through evaporation and sea ice freezing).

In the global configuration, the above equations are solved in the domain Ω, which is limited by three different types of boundaries $\partial\Omega = \bigcup_{i=1}^3 \Gamma_i$. $\Gamma_1 : \{z = 0\}$ stands for the ocean surface, $\Gamma_2 : \{z = -H(\theta, \lambda)\}$ stands for the ocean bottom and Γ_3 stands for the lateral vertical rigid walls. For the dynamical part of the model, the boundary conditions at the surface and the bottom are:

$$A_v \partial_z \mathbf{u} = \tau, \quad p = 0 \text{ on } \Gamma_1, \qquad\qquad (2.4)$$

$$A_v \partial_z \mathbf{u} + A_h \nabla H \cdot \nabla \mathbf{u} = -C_d \mathbf{u}|\mathbf{u}| \text{ on } \Gamma_2, \qquad\qquad (2.5)$$

where τ is the wind stress and C_d is the bottom drag coefficient.

On the vertical rigid walls, no normal flow is allowed. In this configuration of FESOM, no-slip boundary conditions are applied, meaning that the tangential velocity along the vertical wall is zero:

$$\mathbf{u} \cdot \mathbf{n} = 0 \text{ and } \mathbf{u} = 0 \text{ on } \Gamma_3, \tag{2.6}$$

with $\mathbf{n}$ being the unit normal vector to the rigid wall. The vertical velocity w is diagnosed from the continuity equation:

$$\partial_z w = -\nabla \cdot \mathbf{u}, \tag{2.7}$$

which has the following kinematic boundary conditions at the surface and at the bottom:

$$w = \partial_t \eta \text{ on } \Gamma_1, \tag{2.8}$$

$$w = -\nabla H \cdot \mathbf{u} \text{ on } \Gamma_2. \tag{2.9}$$

In the **thermodynamical** part of the ocean model we solve the tracer equations for potential temperature T and salinity S:

$$\partial_t C + \mathbf{v} \cdot \nabla_3 C = \nabla \cdot K_h \nabla C + \partial_z K_v \partial_z C, \tag{2.10}$$

with C standing for T or S and K_h and K_v standing for the lateral and vertical diffusivity for the particular tracer, respectively. The following boundary conditions have to be fulfilled for the tracer equations:

$$K_v \partial_z C = -q, \text{ on } \Gamma_1 \tag{2.11}$$

$$(K_h \nabla C, \ K_v \partial_z C) \cdot \mathbf{n}_3 = 0 \text{ on } \Gamma_2 \cup \Gamma_3, \tag{2.12}$$

where q stands for the surface flux for T and S.

The density ρ is diagnosed via the equation of state according to *Jackett and Mcdougall* (1995):

$$\rho = \rho(T, S, p). \tag{2.13}$$

In the initial state, horizontal velocity is set to zero. The initial conditions for salinity and potential temperature are taken from a climatological data set, which will be discussed later in Section 2.6.

2.1.1   Parameterization of subgrid-scale processes

Mixing from mesoscale eddies in the ocean interior mainly occurs along directions tangent to the local density surface. In this model configuration we employ z-levels, which do not correspond to the isopycnal surfaces. Therefore, the diffusion tensor is rotated to align the diffusive fluxes along the neutral directions according to *Redi* (1982). As the neutral density slope is generally small in the ocean interior, the small slope approximation is applied in the Redi diffusion tensor. *Gent and McWilliams* (1990) also suggested a scheme to parameterize mesoscale eddies by introducing an advective bolus flux. Following these schemes, the right hand side of Equation 2.10 can be rewritten as

$$\nabla \cdot (\mathbf{K}_{redi} + \mathbf{K}_{GM})\nabla_3 C, \tag{2.14}$$

with $\mathbf{K}_{redi}$ and $\mathbf{K}_{GM}$ being symmetric and antisymmetric tensors, respectively. The left term stands for the Redi diffusive flux, while the right term stands for the Gent/McWilliams skew flux (see *Griffies*, 1998). The isopycnal diffusivity and the skew diffusivity are set to the same value of 0.006 ms$^{-1}\Delta$, where Δ is the square root of the surface triangle area. However, the tensor $\mathbf{K}_{redi} + \mathbf{K}_{GM}$ is not bounded as the isoneutral slope increases (e.g. in the mixed layer), which might lead to numerical instabilities. To avoid these instabilities a tapering scheme is applied with a critical neutral slope of 0.004.

Vertical mixing is strong in the surface layers of the ocean and relatively weak below the thermocline; its parameterization in the model is provided by the Pacanowski and Philander scheme (*Pacanowski and Philander*, 1981) which ensures that vertical mixing increases for a weaker stratification. The vertical momentum diffusion coefficient, A_v, and the vertical tracer diffusion coefficient, K_v, are expressed as:

$$A_v = \begin{cases} \frac{v_0}{(1+\alpha \cdot R_i)^n} + A_{v0} & \text{if } R_i > 0, \\ v_0 + A_{v0} & \text{if } R_i \leq 0, \end{cases} \quad (2.15)$$

$$K_v = \begin{cases} \frac{v_0}{(1+\alpha \cdot R_i)^n} + A_{v0} & \text{if } R_i > 0, \\ A_v + K_{v0} & \text{if } R_i \leq 0. \end{cases} \quad (2.16)$$

where v_0, α and n are adjustable parameters set to 10^{-2} m^{2}s^{-1}, 5 and 2, respectively. A_{v0} and K_{v0} stand for the background vertical diffusion for momentum and tracers, respectively, and are set to 10^{-4} m^{2}s^{-1} and 10^{-5} m^{2}s^{-1}. The above formulas depend on the Richardson number R_i, which expresses the ratio of potential to kinetic energy:

$$R_i = \frac{N^2}{(\partial_z u)^2 + (\partial_z v)^2}, \quad (2.17)$$

with N being the buoyancy frequency. The mixing scheme of *Timmermann et al.* (2002) is introduced (a diffusivity of 0.01 m^{2}s^{-1} is applied over a depth defined by the Monin-Obukhov length when it is positive) in order to avoid unrealistically shallow mixed layers in summer.

To reduce dissipation of momentum, the harmonic horizontal viscosity of 2.1 is replaced by a biharmonic one with $B\Delta^3$, where $B = 0.027$ ms^{-1}.

2.2   The sea ice model

Sea ice is an important part of the climate system. First, it affects the heat and mass transfer between the ocean and the atmosphere due to its insulating properties. Second, it influences the radiation balance due to its high albedo, resulting in a high reflection of the incoming solar radiation. Third, the brine release during sea ice formation affects the convection activity in deep water formation areas. Therefore, the coupling of an ocean model with a sea ice model is of high importance if we want to accurately simulate the ocean dynamics.

Sea ice in the model is assumed to be a slab of ice on which snow can

accumulate; on every element of the mesh it is described by the quantities ice thickness, snow thickness, ice concentration and ice velocity. Ice thickness and ice concentration can change due to freezing and melting (thermodynamic processes) and due to deformation, while the ice drift is affected by wind and ocean drag, by the Coriolis force, by the sea surface height gradient and by internal forces within the ice (dynamic processes). In this section the governing equations of the sea ice component of FESOM will be presented, i.e. the continuity equations and the momentum equation, along with a description of the ice thermodynamics (which follow mainly the work by *Parkinson and Washington* (1979) and *Semtner* (1976)) and the ice dynamics (which follow the approaches by *Hunke and Dukowicz* (2001)). A detailed description of the sea ice model can be found in *Timmermann et al.* (2009).

Sea ice consists of individual ice floats which drift freely in regions of low ice concentration or is packed closely in regions of high ice concentration. In order to model sea ice, we consider it as a 2-dimensional continuum. Prognostic variables are:

- effective ice thickness h, defined as the ice volume per area averaged over the ice covered and ice-free part of the element

- effective snow thickness h_s defined in the same way as h

- ice concentration A, a dimensionless quantity ranging from zero to one specifying the fraction of the ice-covered area of an element

- ice (and snow) drift velocity $\mathbf{u}_{ice}$

The evolution in time of the quantities h, h_s and A is described by the continuity equations

$$\partial_t h + \nabla \cdot (\mathbf{u}_{ice} \, h) = S_h, \tag{2.18}$$

$$\partial_t h_s + \nabla \cdot (\mathbf{u}_{ice} \, h_s) = S_s n, \tag{2.19}$$

$$\partial_t A + \nabla \cdot (\mathbf{u}_{ice} \, A) = S_A, \quad 0 \leq A \leq 1, \tag{2.20}$$

where the first and second terms are the derivative in time of the prognostic variable and advection terms, respectively. The terms on the right hand side stand for sources and sinks including freezing and melting (thermodynamic processes), snow fall and snow to ice transformation.

The ice velocity $\mathbf{u}_{ice} = (u_{ice}, v_{ice})$ is computed from the 2-dimensional momentum equation:

$$m\left(\partial_t + f\mathbf{k}\times\right)\mathbf{u}_{ice} = A\left(\tau_{ai} + \tau_{oi}\right) + \mathbf{F} - mg\nabla\eta. \qquad (2.21)$$

It includes the effect of the Coriolis force, the effect of stress due to wind (τ_{ai}) and due to ocean velocity (τ_{oi}), the internal forces ($\mathbf{F}$) and the gravity force on a tilted ocean surface. $m = \rho_i h + \rho_{sn} h_s$ denotes the ice mass per area, where $\rho_i = 910$ kg/m^3 stands for the density of ice. The sea surface height η and the ocean velocity $\mathbf{u}$, which is needed for the computation of τ_{oi}, are taken from the ocean model as part of the coupling scheme.

The process to solve the above equations is the following: First, we solve the momentum equation for ice velocity. Second, the continuity equation is solved by applying a splitting technique: In the advection step preliminary values for sea ice and snow thickness and ice concentration are computed by setting the sources and sinks in equations 2.18-2.20 to zero. Then these variables are updated by accounting for the sources and sinks. In the following, the dynamic and thermodynamic part of the sea ice model will be further described.

2.2.1   Dynamics

The forces appearing in equation 2.21 acting on the sea ice will be further described in this section.

Rheology   The internal forces $\mathbf{F}$ within the sea ice are expressed as the divergence of the stress tensor σ: $\mathbf{F} = \nabla \cdot \sigma$. According to *Hunke and Dukowicz* (1997) we consider the sea ice as a nonlinear elastic viscous compressible fluid. The EVP model consists of the following time-dependent equations, which

have to be solved for $\sigma_1 := \sigma_{11} + \sigma_{22}$, $\sigma_2 := \sigma_{11} - \sigma_{22}$ and σ_{12}:

$$\frac{1}{E}\frac{\partial \sigma_1}{\partial t} + \frac{\sigma_1}{2\zeta} + \frac{P}{2\zeta} = D_D, \tag{2.22}$$

$$\frac{1}{E}\frac{\partial \sigma_2}{\partial t} + \frac{\sigma_2}{2\eta} = D_T, \tag{2.23}$$

$$\frac{1}{E}\frac{\partial \sigma_{12}}{\partial t} + \frac{\sigma_{21}}{2\eta} = \frac{1}{2}D_S. \tag{2.24}$$

D_D, D_T and D_S are the divergence, the horizontal tension and the shearing strain rates, respectively. They depend on the components of the strain rate tensor, $\dot{\epsilon}$, and are defined as

$$D_T = \dot{\epsilon}_{11} + \dot{\epsilon}_{22}, \tag{2.25}$$

$$D_D = \dot{\epsilon}_{11} - \dot{\epsilon}_{22}, \tag{2.26}$$

$$D_S = 2\dot{\epsilon}_{12}. \tag{2.27}$$

The shear viscosity η, the bulk viscosity ζ and Δ are calculated from the formulas

$$\eta = \frac{P}{2\Delta}, \tag{2.28}$$

$$\zeta = \frac{P}{2e^2\Delta}, \tag{2.29}$$

$$\Delta = [D_D^2 + \frac{1}{e^2}(D_T^2 + D_S^2)]^{\frac{1}{2}}, \tag{2.30}$$

where e is an empirical parameter set to 2. The ice strength P depends on the ice concentration A and the ice thickness h:

$$P = P^*h\,\exp(-C(1 - A)), \tag{2.31}$$

with P^* and C being empirical parameters set to 27500 Nm^{-2} and 20, respectively. This formulation ensures that the strength of the ice is high when the ice is thick and when it has a high compactness. An implicit time stepping scheme (backward Euler) is used to solve equations 2.22-2.24.

Shear stresses The wind stress term in equation 2.21 depends on the relative motion between the wind velocity at 10 m height, $\mathbf{u}_{10}$, which is prescribed by atmospheric forcing (see Section 2.6), and the ice velocity:

$$\tau_{ai} = C_{d,ai}\, \rho_a\, \mathbf{u}_{10} |\mathbf{u}_{10}|, \tag{2.32}$$

where $C_{d,ai}$ stands for the ice-atmosphere drag coefficient and $\rho_a = 1.3\,\text{kg/m}^3$ stands for the air density. The ice velocity is small compared to the wind velocity, and is thus ignored in the above equation.

The exchange of momentum between the ocean surface and the sea ice is expressed by

$$\tau_{io} = C_{d,io}\, \rho_0\, (\mathbf{u}_{ice} - \mathbf{u}_s)|\mathbf{u}_{ice} - \mathbf{u}_s|, \tag{2.33}$$

where $C_{d,io}$ stands for the ice-ocean drag coefficient. The ocean surface velocity $\mathbf{u}_s$ is taken from the ocean component as part of the coupling scheme.

2.2.2 Thermodynamics

The ice thermodynamics, i.e. the melting and freezing of sea ice, are based on energy balances for the ice-ocean and ice-atmosphere interface following the work by *Parkinson and Washington* (1979). The heat conductivity of sea ice follows the scheme described by *Semtner* (1976).

Surface energy budget The heat fluxes at the boundary between atmosphere and ocean, and in the ice-covered grid cell between atmosphere and sea ice, are:

$$Q_{ai,ao} = Q_{SW}^{\downarrow} + Q_{SW}^{\uparrow} + Q_{LW}^{\downarrow} + Q_{LW}^{\uparrow} + Q_s + Q_l, \tag{2.34}$$

where Q_{SW} and Q_{LW} stand for the short wave and long wave radiative fluxes, respectively. The symbols $\downarrow$ and $\uparrow$ stand for downwelling and upwelling radiative fluxes, respectively. Q_s and Q_l denote the turbulent fluxes of sensible and latent heat, respectively. In the model, the downwelling shortwave and longwave radiative fluxes are prescribed by the atmospheric forcing, described in Section 2.6. The upwelling shortwave radiation is computed from the down-

welling shortwave radiation, scaled with the albedo α, the reflecting power of a surface:

$$Q^{\uparrow}_{SW} = \alpha \cdot Q^{\downarrow}_{SW}. \tag{2.35}$$

The albedo depends on the surface type and on the surface temperature. Table 2.1 presents the albedo coefficients used in this model configuration.

Table 2.1: Values for the albedo α used in FESOM.

albedo	surface
frozen snow	0.81
melting snow	0.77
frozen ice without snow layer	0.7
melting ice	0.68
open water	0.07

The upwelling longwave radiation is computed based on the Stefan-Boltzmann-Law, which describes the power radiated from a black body in terms of its temperature:

$$Q^{\uparrow}_{LW} = \epsilon \sigma T_s^4, \tag{2.36}$$

with the emissivity ϵ set to 0.97 and being the same for ocean or sea ice surface, and the Stefan-Boltzmann-coefficient being $\sigma =$ 5.67 10^{-8} Wm^{-2}K^{-4}. T_s is the ocean or ice/snow surface temperature.

The turbulent fluxes of sensible and latent heat are calculated from the bulk aerodynamic formulas according to *Parkinson and Washington* (1979):

$$Q_s = \rho_a \, c_p \, C_{e,ao} |\mathbf{u}_{10}| (T_a - T_s), \tag{2.37}$$

$$Q_l = \rho_a \, L \, C_{h,ao} |\mathbf{u}_{10}| (q_a - q_s), \tag{2.38}$$

where c_p stands for the specific heat capacity of water. L stands for the latent heat of vaporization, and in case sea ice exists, it stands for the latent heat of sublimation. L is set to 2.501·10^6J kg^{-1} for evaporation, and to 2.835·10^6 J kg^{-1} for sublimation. The coefficients $C_{e,ao}$ and $C_{h,ao}$ are heat

transfer coefficients for sensible and latent heat, respectively. T_a and q_a are air temperature and specific humidity at 10 m height, and are prescribed by the atmospheric forcing. The air at the surface is assumed to be saturated, and the saturated specific humidity at the surface, q_s, is computed according to *Large and Yeager* (2004) and depends on the the surface temperature T_s:

$$q_s = \frac{q_1}{\rho_a} \exp\left(\frac{q_2}{T_s}\right), \tag{2.39}$$

with q_1=6.89 · 640380 kg/m^3 and q_2=-5107.4 K.

Growth rates for the ice-free area   Every element contains a part which is covered by open water, specified by the ice concentration A. The net heat flux from the atmosphere into the ocean is given by equation 2.34. In equations 2.36 and 2.37, the surface temperature T_s is set to the temperature of the ocean surface layer. In equation 2.35, the albedo is set to the value for open water. If Q_{ao} is negative and the ocean surface temperature is above the freezing temperature T_f[1], the heat flux is used to cool down the ocean surface layer; while a positive value for Q_{ao} would result in a warming of the ocean surface layer. If the ocean surface temperature falls below the freezing temperature T_f, a portion of the water freezes; the growth rate of sea ice measured in meter ice per second is then:

$$(\partial_t h)_{ow} = -\frac{Q_{ao}}{\rho_i L_i}. \tag{2.40}$$

Growth rates for the snow- and ice-covered area   When computing the thermodynamic growth of sea ice in areas which are already ice covered, contributions of ice growth at the ice-atmosphere interface and at the ice-ocean interface have to be summed up.

Considering the ice-atmosphere interface, we have to add to the surface heat budget (equation 2.34) the conductive heat flux Q_c. The conductive heat flux is assumed to be vertically constant and to depend linearly on the

---

[1]The freezing temperature T_f depends according to *Gill* (1982) on the the salinity of the ocean surface layer: $T_f = -0.0575 S_s + 1.7105 \cdot 10^{-3} \sqrt{S_s^3} - 2.155 \cdot 10^{-4} S_s^2$.

temperature difference between the bottom and the surface of the ice/snow. It accounts for both, the snow layer and the ice layer:

$$Q_c = \kappa_i \frac{T_b - T_s}{h_i^*}, \quad \text{with } h_i^* = h_i + h_{sn} \frac{\kappa_i}{\kappa_{sn}} \tag{2.41}$$

with $\kappa_i = 2.1656$ W m^{-1}K^{-1} and $\kappa_{sn} = 0.31$ W m^{-1}K^{-1} being the heat conductivity for ice and snow, respectively. T_b is the temperature at the bottom of the ice and is set to the freezing temperature T_f. The variables $h_i = h/A$ and $h_{sn} = h_s/A$ denote the actual thickness of the ice and snow, respectively. The only unknown in the above equation is the temperature at the surface of the ice (or snow), T_s, which has to be determined from the the surface energy budget:

$$Q_{SW}^{\downarrow} + Q_{SW}^{\uparrow} + Q_{LW}^{\downarrow} + Q_{LW}^{\uparrow} + Q_s + Q_l + Q_c = 0. \tag{2.42}$$

T_s appears in terms 4, 5, 6, and 7. The Newton-Rhapson-Scheme is applied to solve this equation iteratively for T_s. If T_s exceeds the freezing point of freshwater, 0°C, T_s is set to 0°C. After T_s is solved, it is substituted into equation 2.34 to calculate the net heat flux, which will be used to melt ice and snow or form ice. The change of snow and ice thickness is calculated as:

$$\partial_t h_s = -\frac{Q_{ai}}{\rho_{sn} L_i}, \tag{2.43}$$

$$(\partial_t h)_a = -\frac{Q_{ai}}{\rho_i L_i} - \partial_t h_s, \tag{2.44}$$

where $\rho_{sn} = 290$ kg/m^3 is the density of snow. It is assumed that first the total snow layer melts, followed by the ice layer.

On the bottom side of the ice, we assume that melting as well as freezing can occur. The rate of melting or freezing is calculated from the heat flux at the ocean-ice interface Q_{oi}:

$$(\partial_t h)_o = -\frac{Q_{oi}}{\rho_i L_i}. \tag{2.45}$$

The heat flux between ocean and ice is part of the coupling scheme and is

described in Section 2.3.

The ice growth rate depends strongly on the ice thickness. In reality, sea ice ranges from thin to thick ice floes in the area covered by one element in the model. It is thus not reasonable to compute the ice growth rate depending on the effective ice thickness, which presents a mean value over the element. In order to incorporate the dependence of ice growth on ice thickness, seven ice thickness classes ranging from 0 to $2 \cdot h$ are introduced according to the approach by *Hibler* (1984), instead of taking the effective thickness. For every ice class, the ice growth is computed according to equations 2.43, 2.44 and 2.45 and weighted with $\frac{1}{7}$.

Mean growth rates   The above calculated growth rates at the ice surface, the ice bottom and in the open ocean are weighted according to the sea ice concentration. The combined thermodynamic growth rate is then:

$$\partial_t h = A \cdot \left((\partial_t h)_a + (\partial_t h)_o \right) + (1 - A) \cdot (\partial_t h)_{ow} . \qquad (2.46)$$

Updating ice concentration   After computing the thermodynamic growth rates, the ice concentration A is updated according to *Hibler* (1979). In case of freezing, S_A, the term on the right hand side of equation 2.20, is proportional to the area of open water $(1 - A)$:

$$S_A = \frac{1 - A}{h_0} \left\{ (\partial_t h)_{ow} + (\partial_t h)_o \right\}, \qquad (2.47)$$

with h_0 being an empirical parameter, the lead closing parameter, which is set to 0.5 m. In case of ice melting, S_A is determined by the formula

$$S_A = \frac{A}{2h} \left\{ (\partial_t h)_{ow} + (\partial_t h)_a + (\partial_t h)_o \right\}, \qquad (2.48)$$

The updated ice concentration A then equals $S_A \cdot \Delta t$.

2.3   Coupling of the ocean and sea ice components

The ocean and sea ice models are coupled via heat exchange, salt flux due to melting and freezing of ice and snow, and momentum exchange.

The heat flux between ocean and sea ice is given by the formula

$$Q_{oi} = \rho_w \, c_{p,w} \, C_{h,io} \mathbf{u}^*(T_s - T_f), \qquad (2.49)$$

where T_s stands for the ocean surface temperature, $c_{p,w}$ stands for the specific heat capacity of seawater at constant pressure, $C_{h,io}$ stands for the transfer coefficient of the exchange of sensible heat between the ocean and the bottom side of the ice. The friction velocity $\mathbf{u}^*$ is computed as

$$\mathbf{u}^* = \sqrt{C_{d,io}}|\mathbf{u}_s - \mathbf{u}_{ice}|, \qquad (2.50)$$

where $C_{d,io}$ denotes the oceanic drag coefficient and $\mathbf{u}_s$ denotes the ocean velocity of the surface layer.

The salinity of the upper ocean layer is significantly affected by freezing and melting of sea ice. Ice growth is associated with discharge of salt into the ocean layer beneath the ice, which increases the density there. In contrast, ice melting leads to an input of freshwater into the ocean surface layer. In the model, melting and freezing result in a virtual salt flux, which is described by

$$\mathcal{F}_{ice}^{salt} = (S_s - S_{ice})\frac{\rho_i}{\rho_w}(\partial_t h)_{th} + S_s\frac{\rho_{sn}}{\rho_w}(\partial_t h_s)_{th}. \qquad (2.51)$$

The first term describes the salt flux due to thermodynamic changes in the ice thickness, while the second term considers the snow thickness. The ice salinity, S_{ice}, is set to a constant value of 6 psu in the model, with the salinity of snow assumed to be zero.

The difference of precipitation and evaporation $(P - E)$ also provides a source of freshwater. If the air temperature is above the freezing point $(T_a \geq 0°C)$, the precipitation runs completely into the ocean. For $T_a < 0°C$,

the precipitation on the ice-covered area of the grid cell is accumulated as snow. Therefore, the salinity flux due to $P - E$ is given by

$$\mathcal{F}_{P-E}^{salt} = S_s \cdot \begin{cases} P - E & \text{if } T_a \geq 0°C \\ (1 - A) \cdot (P - E) & \text{if } T_a < 0°C \end{cases} \qquad (2.52)$$

The freshwater input due to river runoff is also considered as a virtual salt flux and denoted by $\mathcal{F}_{runoff}^{salt}$.

The total virtual salt flux into the surface layer of the ocean model is

$$\mathcal{F}^{salt} = \mathcal{F}_{ice}^{salt} + \mathcal{F}_{P-E}^{salt} + \mathcal{F}_{runoff}^{salt}. \qquad (2.53)$$

The exchange of momentum between ice and ocean is computed using the formula

$$\tau_{io} = C_{d,io} \, \rho_o \, (\mathbf{u}_{ice} - \mathbf{u}_s) |\mathbf{u}_{ice} - \mathbf{u}_s|, \qquad (2.54)$$

where $C_{d,io}$ stands for the ice-ocean drag coefficient. The stress between the open ocean surface and the atmosphere is

$$\tau_{ao} = \rho_a \, C_{d,ao} \, \mathbf{u}_{10} |\mathbf{u}_{10}|, \qquad (2.55)$$

with the atmosphere-ocean drag coefficient $C_{d,ao}$. The total ocean surface stress is the weighted average of the two terms:

$$\tau_o = A \cdot \tau_{io} + (1 - A) \cdot \tau_{ao}. \qquad (2.56)$$

Drag and transfer coefficients   In this model configuration, the ocean-atmosphere drag coefficient $C_{d,ao}$ and the transfer coefficients for the exchange of sensible and latent heat $C_{e,io}$ and $C_{h,io}$, respectively, are functions of wind speed and the atmospheric stability ζ according to the formulas by

Large and Yeager (2004):

$$C_{d,ao} = \frac{2.7 \cdot 10^{-3}}{\mathbf{u}_{10}} + 0.142 \frac{\mathbf{u}_{10}}{13090}, \tag{2.57}$$

$$C_{e,ao} = \sqrt{C_{d,ao}}, \tag{2.58}$$

$$C_{h,ao} = \begin{cases} 18 \sqrt{C_{d,ao}} & \zeta > 0 \\ 32.7 \sqrt{C_{d,ao}} & \zeta \leq 0. \end{cases} \tag{2.59}$$

The exchange coefficients for the atmosphere - ice interaction are set to constant values:

$$C_{h,ai} = C_{e,ai} = 1.75 \cdot 10^{-3}, \tag{2.60}$$

$$C_{d,ai} = 1.32 \cdot 10^{-3}. \tag{2.61}$$

2.4   Finite element discretization

The equations described above are solved by applying the finite element method (FEM). We will now focus on the ocean component; the application of the FEM to the sea ice equations works analogously. The finite element discretization is explained in more detail in *Danilov et al.* (2004); *Wang et al.* (2008); *Timmermann et al.* (2009).

First, a variational formulation of the governing equation is introduced. We obtain this formulation by multiplying equation 2.1 with a test function $\tilde{\mathbf{u}}$ and integrating it over the domain Ω. By applying integration by parts to the right hand side term, only terms with derivatives up to first order are left. An appropriate function space V for the variational formulation is the Sobolev space $H^1(\Omega)$ of square integrable functions with square integrable weak derivatives of first order. If we apply boundary conditions 2.4-2.6 and assume $\tilde{\mathbf{u}} = 0$ on Γ_3, the problem defined by equation 2.1 can be reformulated

as: Find $\mathbf{u} \in H^1(\Omega)$, such that for each $\tilde{\mathbf{u}} \in H^1(\Omega)$ applies:

$$\int_\Omega [\partial_t \mathbf{u} + \mathbf{v} \cdot \nabla_3 \mathbf{u} + f(\mathbf{k} \times \mathbf{u}) + g\nabla\eta + \frac{1}{\rho_0}\nabla p] \cdot \tilde{\mathbf{u}} \, d\Omega =$$
$$-\int_\Omega [A_h \nabla\mathbf{u} \cdot \nabla\tilde{\mathbf{u}} + A_v \partial_z \mathbf{u} \cdot \partial_z \tilde{\mathbf{u}}] \, d\Omega + \int_{\Gamma_1} \tau\tilde{\mathbf{u}} \, d\Gamma_1 - \int_{\Gamma_2} C_d \mathbf{u}|\mathbf{u}|\tilde{\mathbf{u}} \, d\Gamma_2. \quad (2.62)$$

Similarly, the variational formulation of equation 2.2 is: Find $\eta \in H^1(\Gamma_1)$, such that for each $\tilde{\eta} \in H^1(\Gamma_1)$ applies:

$$\int_{\Gamma_1} \partial_t \eta \, \tilde{\eta} \, d\Gamma_1 - \int_\Omega \mathbf{u} \cdot \nabla\tilde{\eta} \, d\Omega = 0. \quad (2.63)$$

Variables $\mathbf{u}$ and η fulfilling equations 2.62 and 2.63 are called *weak* solutions of the problem given by equations 2.1 and 2.2 and boundary conditions 2.4, 2.5 and 2.6. The formulations 2.62 and 2.63 have to be discretized in order to solve the problem numerically. The functional spaces $V = H^1(\Omega)$ and $W = H^1(\Gamma_1)$ are replaced by finite-dimensional subspaces $V_h \subset V$ and $W_h \subset W$, respectively. The surface and 3D volume are discretized using triangles and tetrahedra, respectively (see Figure 2.1). More details on mesh generation will be given in Section 2.5. The prognostic variables $\mathbf{u}$ and η
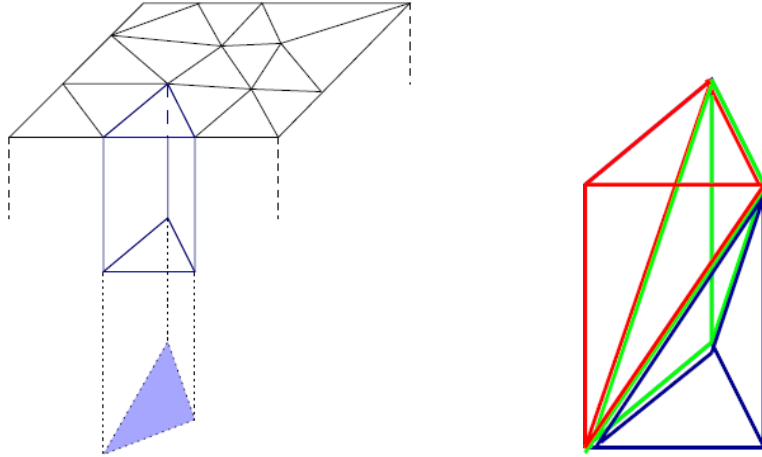

Figure 2.1: Left: The surface triangulation and prisms below each triangle. Right: Decomposition of a prism into three tetrahedrals. [Figures from S. Harig]

are approximated as polynomials using basis functions of the subspaces V_h and W_h, respectively. We employ piecewise linear basis functions in two dimensions $\{M_j\}_{j=1..M}$ for η, while piecewise linear basis functions in three dimensions $\{N_j\}_{j=1..N}$ are used for ocean velocity (the so-called P_1-P_1 discretization), where M and N denote the number of 2D and 3D nodes of the triangulation $\mathcal{T}_h$, respectively. Velocity and sea surface height can thus be approximated as

$$\mathbf{u}_h = \sum_{j=1}^{N}(u_j,\, v_j)N_j, \tag{2.64}$$

$$\eta_h = \sum_{j=1}^{M}\eta_j M_j, \tag{2.65}$$

where u_j, v_j and η_j denote the model values for velocity and sea surface height in node j. Basis functions M_j and N_j equal one in node j and go linearly to zero at neighboring nodes. The discrete expressions for velocity and sea surface height, $\mathbf{u}_h$ and η_h, are now inserted into equations 2.62 and 2.63. This approach is called *Galerkin*-method. As test functions we choose the basis functions of the discrete subspaces V_h and W_h. This approach leads to large systems of linear equations, which are solved iteratively for the nodal values u_j, v_j and η_j. After obtaining discrete solutions for horizontal velocity and sea surface height, we solve for the vertical velocity w. The equation involves first order derivatives. A numerical solution of this equation leads to difficulties, and in order to avoid these problems, we introduce a new variable, the vertical velocity potential Φ, such that $w = \partial_z \Phi$. The variational formulation of equation 2.7 is then: Find $\Phi \in H^1(\Omega)$, such that for each $\tilde{\Phi} \in H^1(\Omega)$ applies:

$$\int_{\Omega} \partial_z \Phi \partial_z \tilde{\Phi}\, d\Omega = -\int_{\Omega} \mathbf{u} \cdot \nabla \tilde{\Phi}\, d\Omega \tag{2.66}$$

The potential Φ is approximated in the finite element sense as

$$\Phi_h = \sum_{j=1}^{N} \Phi_j N_j, \tag{2.67}$$

with nodal values Φ_j. After computing Φ_h, the vertical velocity w is obtained as an element-wise constant function.

The remaining equations for tracers (eq. 2.10) are solved in a similar manner, i.e. setting up the variational formulation, discretizing this formulation with the Galerkin method, and solving the resulting large systems of linear equations. With T and S obtained, the nodal values of the density are computed via the equation of state (eq. 2.13). Then the hydrostatic pressure is computed from equation 2.3 considered in the finite difference sense.

Time stepping scheme of the ocean component   In the model, time stepping of the momentum equation works in the following way: As explicit Coriolis and vertical viscosity terms can limit the possible time steps in some situations, we treat the Coriolis term semi-implicitly (by estimating this term as a weighted sum over steps $n+1$ and n) and the vertical viscosity term implicitly. The elevation term is also treated implicitly; this has the advantage that it suppresses gravity waves.

Solving the dynamic part of the ocean model with the standard Galerkin method leads to major numerical problems, which are associated with the advection-dominated flow with high Reynolds numbers on the one side and the possibility of pressure modes because of using the same horizontal test functions for velocity and elevation on the other side. To overcome these problems, the *characteristic Galerkin* and *pressure projection methods* are introduced.

Before starting the iteration, potential temperature and salinity are initialized by setting them to climatological values; furthermore velocity is initialized by setting it to zero. Before each iteration step, the atmospheric forcing data is read in. The dynamics and thermodynamics are staggered in time by one half time step. First, density and hydrostatic pressure are

computed from salinity and potential temperature. The solution of the horizontal momentum and continuity equation is performed in three steps with the *pressure-projection method*, which is a predictor-corrector-method:

(i) in the predictor step, an auxiliary horizontal velocity $\mathbf{u}^*$ is calculated,

(ii) then the sea surface height is determined,

(iii) in the correction step the correct velocity is determined.

Next, the vertical velocity is computed by determining the vertical velocity potential. As a last step, tracer equations are solved for potential temperature and salinity. Tracer advection is solved with the flux-corrected-transport (FTC) method. The time stepping scheme of the ocean component is described in more detail in *Wang et al.* (2008).

Time stepping scheme of the coupled ocean-ice model After the initialization of ocean and ice variables, the atmospheric forcing data is read in. Every iteration step of FESOM consists of the following steps:

(i) In the *ocean to ice*-coupling routine, the variables potential temperature, salinity and horizontal velocity of the ocean surface layer, T_s, S_s, and $\mathbf{u}_s$, and the sea surface height η are handed over to the sea ice component.

(ii) One time step of the sea ice model is performed, resulting in variables ice concentration A, thickness h and snow thickness h_s.

(iii) In the *ice to ocean*-coupling routine, the fluxes of heat, freshwater and momentum are handed over to the ocean component.

(iv) One time step of the ocean model is performed, resulting in variables horizontal ocean velocity $\mathbf{u}$, vertical ocean velocity w, potential temperature T, salinity S, density ρ, pressure p and sea surface height η.

2.5   Mesh generation

In order to numerically solve the governing equations with the finite element method, a triangulation of the model domain Ω is needed. Here, the triangulation consists of triangular elements on the ocean surface and of tetrahedral elements in the 3D domain. First, a triangular unstructured 2D surface mesh is generated. In this work the surface mesh is generated with the software package Triangle (*Shewchuk*, 1996). The mesh quality, i.e. the extent in which the triangle resembles an equilateral triangle, is further improved by several relaxation methods. Also, there has to be a transition zone between areas of high and coarse resolution. Then the 3-dimensional mesh is generated by cutting the volume into horizontal layers, the z-layers. The resulting prisms are then divided into three tetrahedral elements. 3D nodes are always aligned vertically below the 2D surface nodes.

In this work, the model domain covers the global oceans. For the surface mesh, we use a nominal horizontal resolution of 1.5° throughout most of the world's ocean; resolution is doubled along the coastlines and further improved to 24 km north of 50°N. The two major CAA straits are artificially widened to allow for the presence of at least three grid points; this approach is similar to the one used in traditional climate models. A second surface mesh was produced, with a further refinement up to 5 km in the CAA (depicted in Figure 2.2). The two surface meshes are denoted by LOW and HIGH, and their resolution is given in Table 2.2. Fury and Hecla Strait connecting the CAA and Foxe Basin (with a width of 2 km) is closed in our model. In the vertical both meshes have 55 z-levels with thickness of 10 m in the top 100; vertical resolution is gradually increasing downwards (see Table A1 in the appendix). The model bathymetry is taken from the IBCAO data (*Jakobsson et al.*, 2008) for the Arctic region and from the 1 min resolution GEBCO data for other regions. A linear combination of the two datasets is taken between $64°N$ and $69°N$. To avoid the north pole singularity, rotated coordinates with the north pole displaced to Greenland are used.
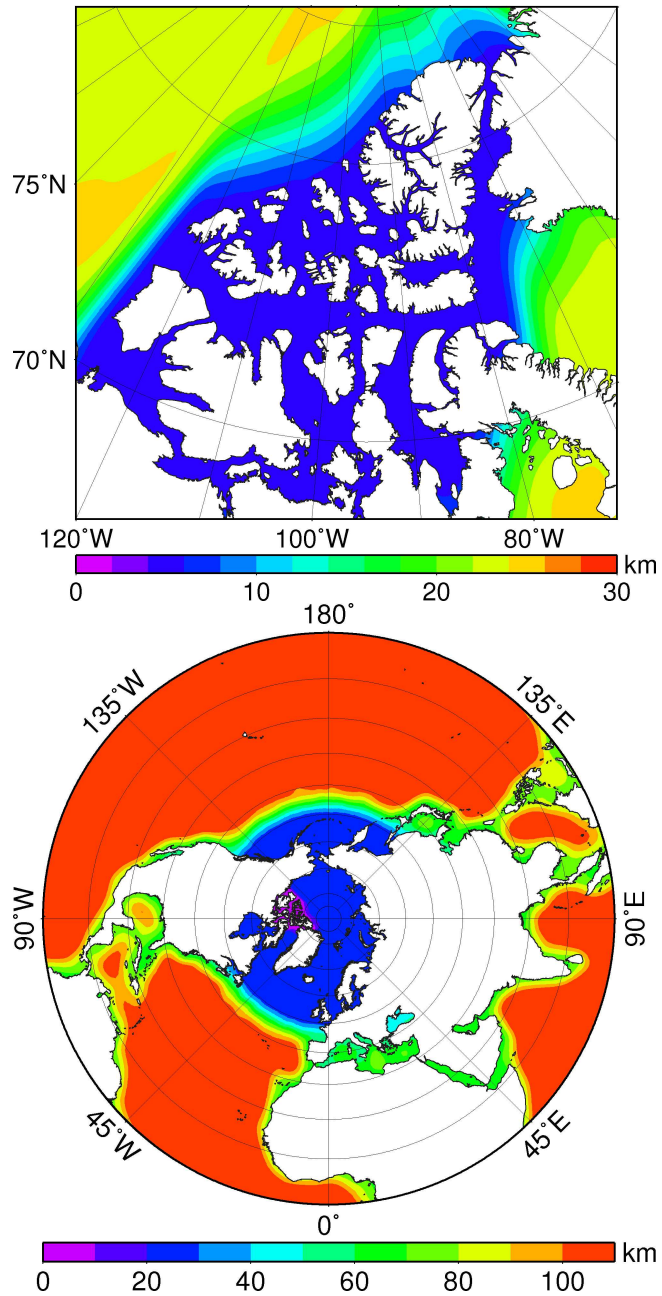
Figure 2.2: Resolution in km of the global mesh in the CAA area (top) and in the northern hemisphere (bottom).

Table 2.2: Resolution of the unstructured meshes.

	HIGH	LOW
CAA	5 km	24 km
north of 50°N	24 km	24 km
globally	$1.5° \cdot 1.5° \cos(\text{lat})$	$1.5° \cdot 1.5° \cos(\text{lat})$

2.6   Model setup and atmospheric forcing

This configuration of FESOM is forced by atmospheric data taken from the Common Ocean-Ice Reference Experiment version 2 data set (CORE-II, *Large and Yeager*, 2008). The forcing fields used in FESOM are listed in Table 2.3. The CORE-II data is provided on the T62 grid (with a zonal resolution of approximately 1.875 degree). Figure 2.3 shows the mean temperature and wind field in the CAA region in winter and summer from the CORE-II dataset. In winter, temperatures are extremely low, up to -36°C, while in summer temperature rises above the freezing point in the southern part of the CAA.

Table 2.3: Atmospheric forcing fields taken from CORE-II (*Large and Yeager*, 2008) used in this FESOM configuration.

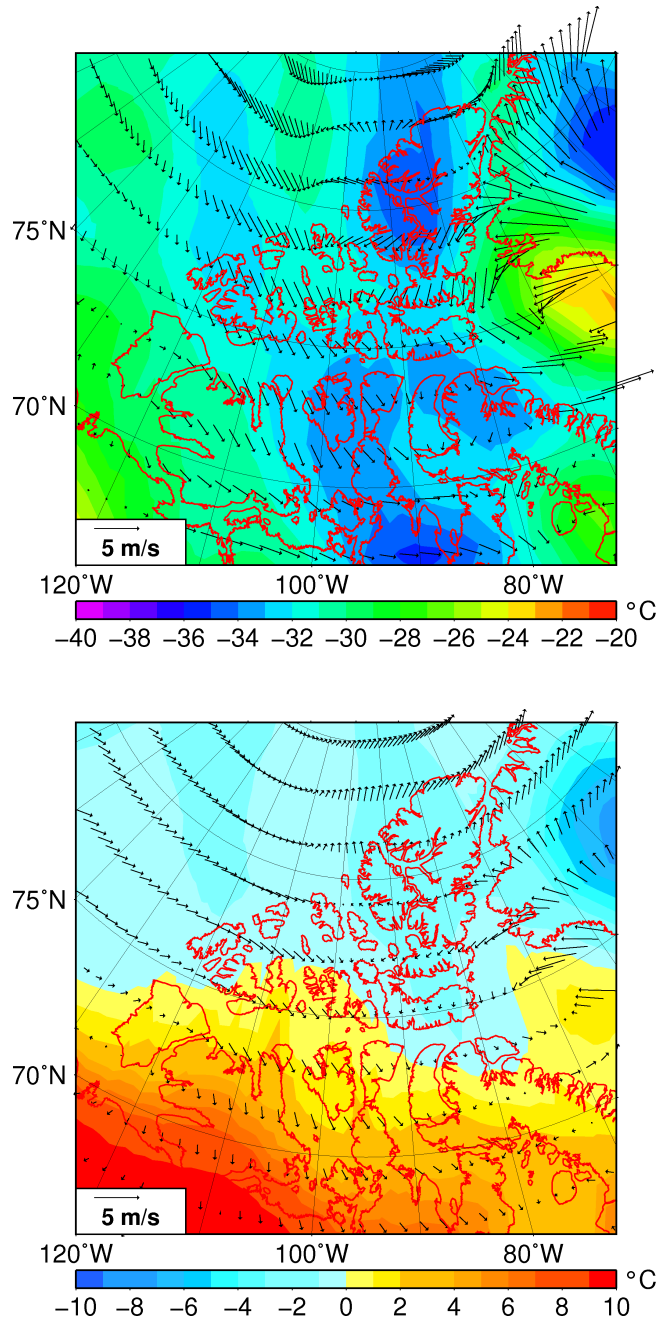| variable	unit	resolution in time
10m zonal wind	m/s	6-hourly
10m meridional wind	m/s	6-hourly
10m air temperature	K	6-hourly
10m specific humidity	kg/kg	6-hourly
precipitation	mm/s	monthly
downward shortwave radiation	W/m^2	daily
downward longwave radiation	W/m^2	daily

Figure 2.3: Mean air temperature and wind field at 10 m height in the CAA region from the CORE-II data set for January (top) and July (bottom) 1958-2007. The temperature is shown by color patches, and the wind field is shown by arrows.

River runoff was taken from the dataset described in *Dai et al.* (2009), which contains the monthly streamflow at the farthest downstream stations of the world's 925 largest ocean-reaching rivers.

Two hindcast simulations were carried out with the only difference being the horizontal resolution in the CAA region. The simulations were initialized with the mean temperature and salinity fields from the Polar Hydrography Center global ocean climatology version 3 (PHC 3.0, *Steele et al.*, 2001). The initial sea ice concentration and thickness were taken from the long term mean of a previous simulation. A sea surface salinity restoring to the monthly PHC 3.0 climatology with a piston velocity of 10 m per 60 days was applied. The model was integrated for the time period 1958-2007 and the last 40 years are used in the analysis. Monthly mean and for some time periods daily fields of the prognostic variables were saved for analysis.

2.7   Computation of transports

Volume transport is calculated by integrating normal velocity $\mathbf{u} \cdot \mathbf{n}$ over a vertical cross section of area A:

$$T_{vol} = \int_A \mathbf{u} \cdot \mathbf{n} \, dA. \tag{2.68}$$

Freshwater transport through a cross section of area A is calculated relative to $S_{ref} = 34.8$ psu, which is the mean salinity of the Arctic Ocean (*Aargaard and Carmack*, 1989):

$$T_{liqfw} = \int_A \frac{S_{ref} - S}{S_{ref}} \mathbf{u} \cdot \mathbf{n} \, dA. \tag{2.69}$$

Sea ice volume transport is calculated as:

$$T_{ice} = \int_l h \frac{\rho_i}{\rho_w} \cdot \mathbf{u}_{ice} \cdot \mathbf{n} \, dl, \tag{2.70}$$

with the ice density $\rho_i = 920$ kg m^{-3} and water density $\rho_w = 1000$ kg m^{-3}. Freshwater transport in form of sea ice is computed by multiplying T_{ice} with

$(S_{ref} - S_{ice})/S_{ref}$, where $S_{ice} = 6$ mSv.

The liquid freshwater content h_{fw} at a particular grid point is defined as the depth integrated salinity anomaly relative to $S_{ref} = 34.8$ psu, integrated from the surface to a depth of 500 m:

$$h_{fw} = \int_{z=0m}^{500m} \frac{S_{ref} - S}{S_{ref}} \, dz. \tag{2.71}$$

To obtain a time series of the liquid freshwater content in a region Ω we spatially integrate h_{fw}:

$$FWC_{liq} = \int_{\Omega} h_{fw} \, d\Omega. \tag{2.72}$$

In this work the Arctic region is defined by Davis Strait, Fram Strait, Bering Strait and Barents Sea Opening.

The sea ice freshwater content of the Arctic Ocean is calculated as:

$$FWC_{ice} = \frac{S_{ref} - S_{ice}}{S_{ref}} V_{ice}, \tag{2.73}$$

where V_{ice} is the sea ice volume. Again we consider here the area of the Arctic Ocean bounded by the straits mentioned above.

The streamfunction of meridional overturning circulation at a given latitude θ and time t is computed by zonally and vertically integrating the meridional velocity v:

$$T_{overt}(\theta, z, t) = \int_{z}^{0} \int_{\phi_{west}}^{\phi_{east}} v(\phi, \theta, z', t) \, d\phi \, dz'. \tag{2.74}$$

Chapter 3

Model assessment in the Arctic Ocean and CAA

We now assess the model performance, by focusing on sea ice conditions in the Arctic Ocean (Section 3.1), on the freshwater (FW) budget of the Arctic Ocean (Section 3.2) and on the ocean dynamics of the CAA (Section 3.3). In this chapter, we only analyze model results from the simulation with highly resolved CAA (simulation HIGH, see Table 2.2).

3.1 Arctic Ocean sea ice

Figure 3.1 shows the simulated sea ice extent (defined as the total area of grid cells with at least 15% sea ice concentration) in the northern hemisphere together with satellite passive microwave data from NSIDC (*Fetterer et al.*, 2009). The sea ice extent exhibits a strong seasonal cycle with peaks in March and minimum in September. For the period 1979-2007, the mean March (September) ice extent amounts to 15.76 $\cdot 10^6$ km^2 (7.58 $\cdot 10^6$ km^2) and 15.58 $\cdot 10^6$ km^2 (6.74 $\cdot 10^6$ km^2) for model and observation, respectively, revealing that the summer ice extent is slightly overestimated by the model. There is a strong decrease in the sea ice extent over the time period. For the period 1990-2007, the modeled and observed March (September) ice extent decreases by 0.42 $\cdot 10^6$ km^2 (0.89 $\cdot 10^6$ km^2) and 0.56 $\cdot 10^6$ km^2 (0.94 $\cdot 10^6$ km^2)

per decade, respectively. The 2007 summer minimum is well represented in the model. The root mean square error of modeled ice extent is E=0.27 $\cdot 10^6$ km^2, while the correlation coefficient between the modeled and observed sea ice extent anomalies is r=0.87 (N*=9, significance 99%; the significance level for the correlation is computed from the effective degrees of freedom based on the formula by *Chelton* (1983)).
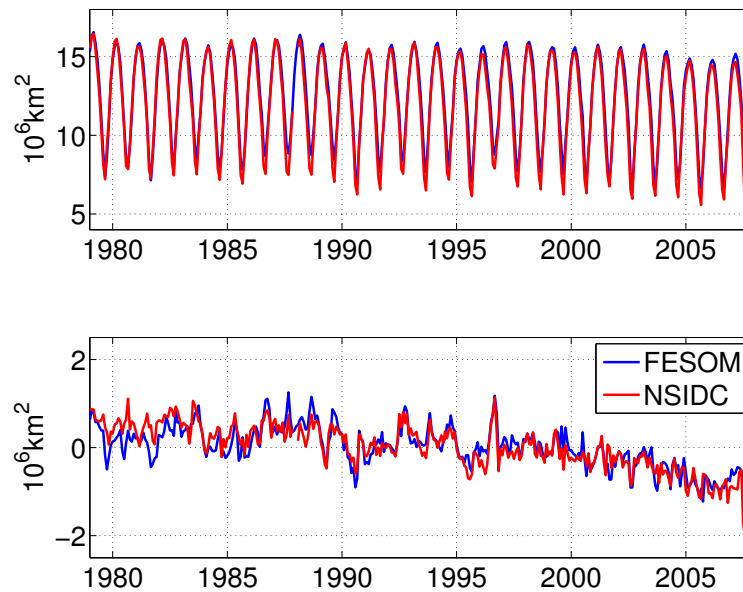

Figure 3.1: Mean monthly sea ice extent (top) and its anomaly (bottom) from the model (blue) and satellite observation (red). The anomaly is calculated by subtracting the mean seasonal cycle from the time series.

During the ten ICESat campaigns between 2003 and 2008 measurements of sea surface elevation were conducted in the Arctic Ocean. Each of the campaigns lasted ∼34 days and was conducted during different time periods in spring and autumn. Based on these measurements, *Kwok and Cunningham* (2008) computed the ice freeboard and then estimated the ice thickness, the mean of which is depicted in Figure 3.2 together with the model results. As shown by both the observation and model results, the sea ice is the thickest along the northern CAA and Greenland coast and declines toward the Siberian shelf. The model underestimates the ice thickness north of the CAA

in both seasons. In spring, it slightly overestimates the ice thickness on the Siberian shelf. In autumn, it underestimates the ice thickness in the Eurasian Basin. The root mean square error between modeled ice thickness and observations amounts to E=0.54 m for spring and E=0.72 m for autumn. Considering large uncertainties in the observations (∼0.7 m, according to *Kwok and Cunningham* (2008)), the model reasonably reproduced the observed spatial and seasonal variation in sea ice thickness.
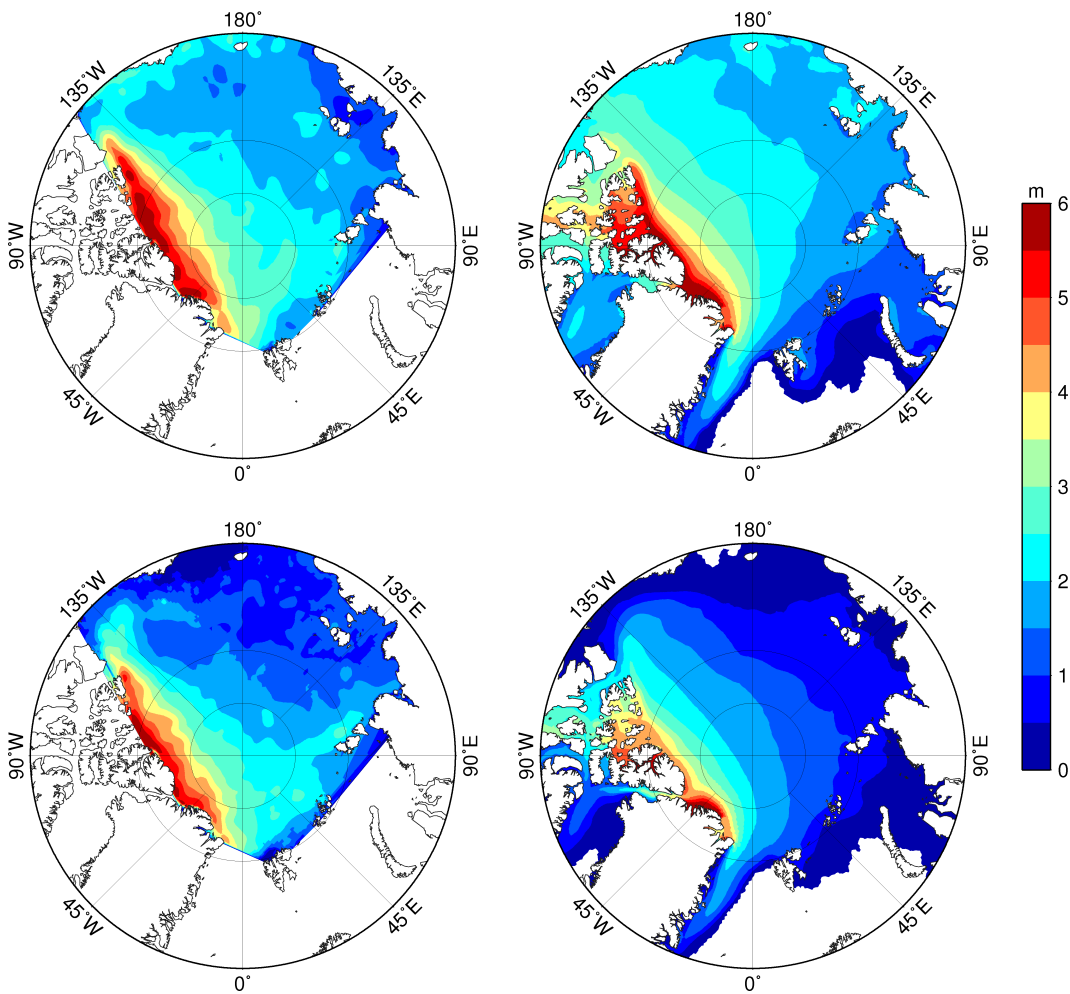

Figure 3.2: Mean sea ice thickness for spring (top) and autumn (bottom) from ICESat measurements (*Kwok and Cunningham*, 2008) (left) and from FESOM simulations (right). The spring and autumn means were calculated by taking into account all available datasets for 2003-2007. The same time periods are used for deriving the model results.

3.2   Freshwater budget of the Arctic Ocean

3.2.1   Transports across the main gates of the Arctic Ocean

Table 3.1 provides means of volume, liquid freshwater and sea ice transports through the main gates of the Arctic Ocean derived from FESOM for the time period 1968-2007. The table also shows observational estimates for these straits. Freshwater transports were calculated with a reference salinity of $S_{ref} = 34.8$ psu, which is the mean salinity of the Arctic Ocean (*Aargaard and Carmack*, 1989).

Davis Strait, located between Baffin Island and Greenland, is characterized by two currents with opposite directions: The northward flowing West Greenland Current (WGC) at the eastern side of the strait is relatively warm and salty, while the southward flowing Baffin Island Current (BIC) at the western side is relatively cold and fresh. The BIC combines the CAA outflow of Arctic origin with the warmer WGC waters. The mean Davis Strait liquid freshwater transport in the model is 110.6 mSv, well comparable to observation. The mean volume transport in the model is 1.81 Sv, lower than observed mean values, but still in the uncertainty range.

Fram Strait is the only deep connection between the Arctic Ocean and the North Atlantic (*Schauer et al.*, 2008). The East Greenland Current (EGC) carries fresh and cold Arctic waters and sea ice southward, while the West Spitzbergen Current (WSC) carries warm Atlantic waters into the Arctic Ocean. Simulated net volume (1.34 Sv) and liquid freshwater (56.1 mSv) transports through Fram Strait agree well with the observations; the modeled southward and northward transports are, however, much lower than observations. *Schauer et al.* (2008) observed a 12 Sv northward flow and a 14 Sv southward flow, whereas FESOM simulates 3.3 Sv northwards and 4.6 Sv southwards at the observation section at 79°N. The underestimation of the magnitude of transports through Fram Strait was shown in other models as well (*Lique et al.*, 2009; *Jahn et al.*, 2009) and the reason might partly be that the retroflection point of the Atlantic current is too far to the south in

simulations. Fram Strait is the main Arctic sea ice export route. Although the model very well represents the sea ice extent and thickness, the volume export is overestimated compared to available observations.

Table 3.1: Simulated volume and freshwater budget of the Arctic Ocean for the time period 1968-2007 and observational estimates. Liquid freshwater transports are given in mSv with a reference salinity of S_{ref}=34.8 psu, volume transports in Sv and ice transports in mSv. For observations, net transports are given, unless otherwise noted. Standard deviations are calculated from annual mean net fluxes. Fluxes into the Arctic Ocean have a negative sign, and vice versa.

Budget term	FESOM				Obs.
	Inflow	Outflow	Net	Std	
Vol. transports					
Fram Strait	-3.28	4.62	1.34	0.43	[1]2±2.7
Davis Strait	-0.64	2.45	1.81	0.31	[2]2.6±1, [3]2.3± 0.7
Bering Strait	-0.65	0.01	-0.64	0.08	[4]-0.8±0.2
Barents Section	-3.0	0.53	-2.46	0.38	[5]-1.8
Liq. FW transports					
Fram Strait	8.7	47.3	56.1	9.2	[6]84±17
Davis Strait	-13.5	124.1	110.6	17.2	[2]92±34, [3]116±41
Bering Strait	-52.5	0.9	-51.6	6.6	[6]-76±10
Barents Section	6.6	2.6	9.2	3.8	[6]3±3
Ice Exports					
Fram Strait			111.0	19.8	[6]73±11
Davis Strait			24.0	4.8	[2]17
Bering Strait			-0.6	2.4	
Barents Section			8.2	4.9	

[1]*Schauer et al.* 2008 (1997-2007), [2]*Cuny et al.* 2005 (09/1987-08/1990), [3]*Curry et al.* 2011 (08/2004-09/2005), [4]*Woodgate et al.* 2010 (1991-2007), [5]*Skagseth et al.* 2008 (1997-2006), [6]*Serreze et al.* 2006. Numbers in brackets denote the time period of observations.

The Barents Sea receives salty water through the Barents Sea Opening, contributing to a small net freshwater outflow as indicated in both model simulations and observations.

Bering Strait is the only connection of the Arctic Ocean with the Pacific Ocean, and is ∼85 km wide and ∼50 m deep (*Woodgate et al.*, 2010). Pacific waters entering through Bering Strait present an important source of freshwater to the Arctic Ocean. The Bering Strait freshwater inflow accounts for 30 % of the total Arctic Ocean freshwater sources (*Serreze et al.*, 2006). The model slightly underestimates the Bering Strait volume and freshwater inflow because of the coarse (24 km) resolution used in this region.

3.2.2   Arctic Ocean freshwater content

Compared to adjacent oceans the Arctic Ocean stores a large amount of freshwater, including both liquid water and sea ice. The liquid part of the freshwater is concentrated in the surface layers leading to a strong density stratification defined mostly by salinity.

Figure 3.3 depicts the interannual variability of liquid freshwater content (LFWC) and sea ice volume simulated by FESOM. The LFWC was calculated relative to 34.8 psu and was integrated from the surface to a depth of 500 m. The LFWC simulated by FESOM has local maxima in the years 1973, 1981, 1990 and 2000, which is comparable to those simulated by *Köberle and Gerdes* (2007) (1970, 1982 ,1990 and 2000) and by *Lique et al.* (2009) (1966, 1981, 1988, 2001). The recent increase in LFWC, also shown by *Rabe et al.* (2011), is represented in the model.

The variability in LFWC is strongly linked to freshwater exports of the Arctic Ocean (shown in Figure 3.4). The changing rate of the LFWC and the total export rate through the main gates of the Arctic Ocean are relatively well correlated (r=-0.57, N*=12, significance 94%). A decrease in the Arctic Ocean freshwater content is associated with increased exports of freshwater. The correlation of the changing rate of LFWC with FW exports through Davis Strait is the highest (r=-0.66, N*=12, significance 98%, not shown in the figure), but not significant for Fram Strait FW export (r=0.18). This

points out the importance of liquid freshwater exports through the CAA in determining the changes in the Arctic freshwater content.

The simulated sea ice volume (Figure 3.3) has local maxima in the late 1970's and late 1980's, and is decreasing from then on. This is similar to the model results described by *Lique et al.* (2009) and *Rothrock and Zhang* (2005). A change in sea ice volume must result from changes in sea ice export and sea ice production (freezing minus melting). The study by *Rothrock and Zhang* (2005) showed that sea ice production is most strongly controlled by temperature over the entire Arctic basin, whereas the sea ice export through Fram Strait (which dominates the overall Arctic Ocean sea ice export) is controlled by local winds. In our simulation, there is no significant correlation between changing sea ice volume and the Arctic Ocean sea ice export (r=-0.18, time series not shown). Melting and freezing of sea ice in the interior of the Arctic appears to be the most important in determining the ice volume variability (r=0.52, N*=34, significance 99%, time series not shown).
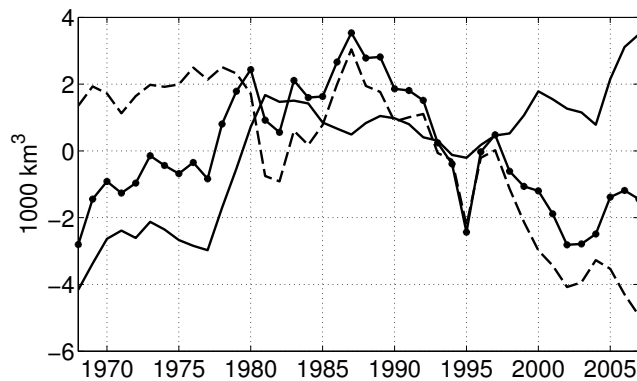

Figure 3.3: Time series of simulated annual mean liquid freshwater content anomaly of the Arctic Ocean from the surface to 500m depth (solid), sea ice volume anomaly (dashed) and their sum (solid line with dots). The Arctic Ocean is defined as the region bounded by Davis Strait, Fram Strait, Bering Strait and Barents Section.
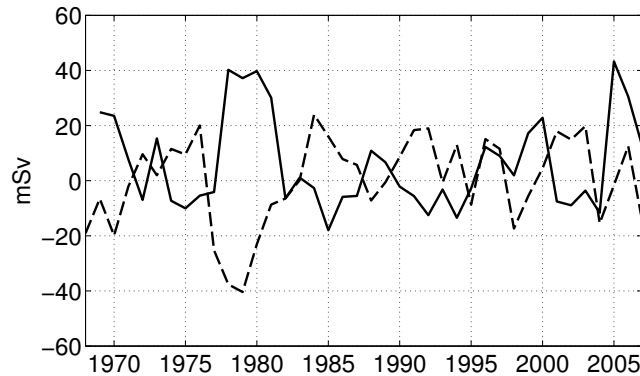
Figure 3.4: Time series of the simulated changing rate of annual mean liquid freshwater content in the Arctic Ocean (solid) and the anomaly of the total freshwater flux through all the Arctic Ocean gates (dashed).

3.3   The simulated CAA ocean dynamics

In this section we concentrate on the circulation pattern in the CAA region (Section 3.3.1), volume and freshwater transports through the CAA's main straits including a comparison with available observational data (Sections 3.3.2-3.3.4) and the constituents of the freshwater transport variability (Section 3.3.5). Section 3.3.6 summarizes the main findings of the CAA throughflow analysis.

3.3.1   Mean sea surface height and circulation in the CAA region

The simulated sea level is higher in the Arctic Ocean than in Baffin Bay (Figure 3.5b), due to lower salinity and thus lower density of the surface layer in the Arctic Ocean. This results in a net outflow from the Arctic Ocean to Baffin Bay. Along with the sea surface height (SSH) gradient between the Arctic Ocean and Baffin Bay, there is a gradient of SSH across the main straits of the CAA: In Parry Channel SSH is higher on the southern side of the strait, in Nares Strait SSH is higher on the western side of the strait. Over the CAA, the SSH is the highest in the west and decreases to the east.
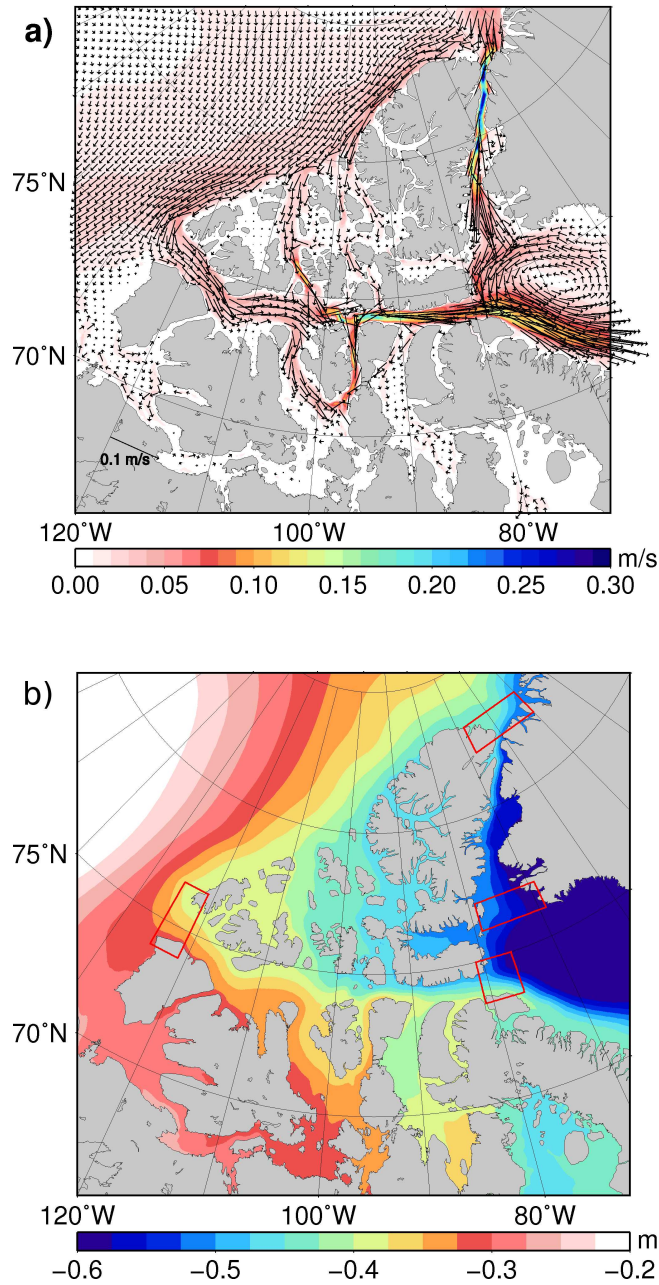
Figure 3.5: (a) Mean simulated horizontal velocity at 50 m depth and (b) mean simulated sea surface height relative to the global mean for the time period 1968-2007. Red boxes in (b) indicate areas over which SSH is averaged (see Section 4.1).

Figure 3.5a depicts the simulated mean horizontal velocity field at 50 m depth. In the Canadian Basin of the Arctic Ocean there is an anticyclonic circulation transporting Upper Halocline Waters (UHW) along the Canadian Arctic shelf westwards. This anticyclonic circulation is confined to the top 200 m, and partly enters the CAA through Nares Strait, the channels between the Queen Elizabeth Islands and McClure Strait. Below this anticyclonic current, a cyclonic undercurrent with its core at around 500 m (in our simulation) transports Lower Halocline Waters (LHW) eastwards (not shown; see *Aksenov et al.*, 2010, for the definition of water masses). The simulated mean velocity at 50 m depth is highest in the eastern Parry Channel and in the northern Nares Strait where the straits are narrow. Regarding Parry Channel, the maximum velocity of 22 cm/s is reached north of Prince of Wales Island. In Nares Strait a maximum velocity of 31 cm/s is reached in its northern end, in Robeson Channel. At the same location *Münchow and Melling* (2008) observed velocities exceeding 40 cm/s at around 100 m depth in August 2003, with the simulated velocity in this particular month being 57 cm/s at 100 m depth. Arctic waters exiting the CAA through Lancaster, Jones and Smith Sounds enter the North Atlantic through Baffin Bay. They remain confined to the western side of Baffin Bay where they feed the Baffin Island Current.

3.3.2   Parry Channel

Parry Channel is the main passage connecting the Beaufort Sea in the west with Baffin Bay in the east. It comprises (from west to east) McClure Strait, Viscount Melville Sound, Barrow Strait and Lancaster Sound. McClure Strait is one of the major entrances to Parry Channel, apart from Byram Martin and Penny Straits at its northern side and McClintock Channel, Peel Sound and Prince Regent Inlet at its southern side (Figure 1.1). There is a net flow from west to east, with the largest amount of water entering through McClure Strait (see discussion later in this section). There is also a cyclonic circulation around Prince of Wales Island with a southward flow in McClintock Channel and northward flow reentering Parry Channel through

Peel Sound (see Figure 3.5a). This cyclonic current loop results partly from sills located south of Prince of Wales Island and in Barrow Strait which restrain further westward flow (*Wang et al.*, 2012a). The northward transport through Peel Sound was estimated as 0.17 Sv for April 1981 by *Prinsenberg and Bennet* (1989). Our simulated value is 0.20 Sv for the same time period.

Table 3.2: Mean transports through the CAA. FESOM output is given for the time period 1968-2007. FW transports are given in mSv with a reference salinity of S_{ref}=34.8 psu. Standard deviations are calculated from annual mean net fluxes. HG & CS stands for Hell Gate and Cardigan Strait.

Budget term	FESOM		Obs.
	Net	Std	
Vol. Transports (Sv)			
Lancaster Sound	0.86	0.16	[1]0.46±0.09, [1*]0.53, [2]0.68
Nares Strait	0.91	0.16	[3] 0.57±0.09
HG & CS	0.04	0.01	[4]0.2/0.1 for CS/HG
Liq. FW Transports (mSv)			
Lancaster Sound	71.36	12.82	[1]32±6, [5]45 ±15
Nares Strait	47.87	7.89	
HG & CS	3.46	0.52	
Ice Exports (mSv)			
Lancaster Sound	4.16	1.07	[1]2.1, [6]2.7
Nares Strait	5.26	1.63	
HG & CS	0.13	0.07	

[1]*Peterson et al.* 2012 (1998-2011), [1*]*Peterson et al.* 2012 (1998-2006), [2]*Prinsenberg et al.* 2009 (1998-2006), [3] *Münchow and Melling* 2008 (Aug 2003 to Aug 2006, excluding the top 30 m), [4]*Melling et al.* 2008, [5] *Prinsenberg and Hamilton* 2005 (1998-2001, excluding the top 30 m), [6] *Agnew et al.* 2008 (2002-2007). Numbers in brackets denote the time period of observations.

Since 1998 the Bedford Institute of Oceanography operates an array of moorings (*Peterson et al.*, 2012) in western Lancaster Sound. At the location of the mooring array, western Lancaster Sound has a maximum depth of 285 m and a width of 68 km. This geometry is well resolved in the model (max. depth: 270 m, width: 71 km). Figure 3.6 depicts a comparison of monthly mean net volume and freshwater transport of the observational data with model output.
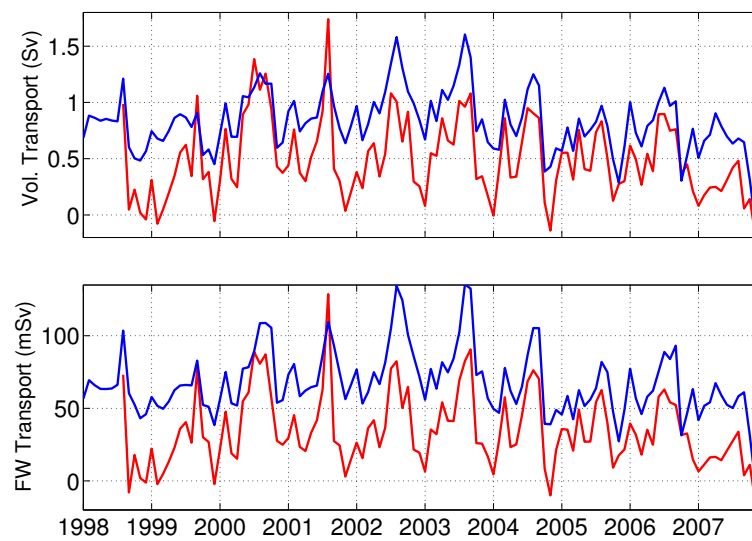

Figure 3.6: Volume (top) and freshwater (bottom) transports through western Lancaster Sound from observations (red, *Peterson et al.* 2012) and FE-SOM (blue).

The model result and the observation are highly correlated (r=0.81, N*=20, significance 99% and r=0.82, N*=19, significance 99%, for volume and freshwater, respectively) and have a root mean square error of 0.35 Sv (volume transport) and 37 mSv (freshwater transport). The fact that we find the highest correlation at zero time lag indicates that the model simulates the seasonal cycle quite well: Both the simulated volume and freshwater transport shows a maximum in August, as observed. In contrast, *McGeehan and Maslowski* (2012) found the maximum volume transport through Lancaster Sound to occur in March, and the maximum freshwater transport to occur in August (based on their modeling study). The strength of the variability

is captured very well by our model, as indicated by the standard deviation (σ=0.35 Sv and σ=25 mSv for the observed volume and freshwater transport, respectively, and σ=0.27 Sv and σ=23 mSv for the simulated time series). The observational transport covers the whole depth of the cross section, although Icycler profilers captured the shallow depths only for some years. Therefore, CTD data at 40 m depth had to be extrapolated to the surface for approximating the freshwater transport when Icycler profilers were absent (*Peterson et al.*, 2012). Another source of uncertainty in the observations is the sparseness of the mooring array (*Peterson et al.*, 2012), consisting of four moorings during the period 2001-2006 and only two moorings during the periods 1998-2001 and 2006-2011. The observational transport depends on the weighting of the individual moorings. The mean Lancaster Sound volume transport of 0.68 Sv for the period 1998-2006 estimated by *Prinsenberg et al.* (2009) was revised to a new estimate of 0.53 Sv by using a different weighting (*Peterson et al.*, 2012). These uncertainties in observations make the quantitative comparison with model results very difficult.

The time series of simulated annual mean volume, freshwater, and sea ice transport through western Lancaster Sound are shown in Figure 3.7. The simulated volume transport has local maxima in the years 1984, 1989, 1997 and 2002, and local minima in 1981, 1995 and 1999, which are comparable to those simulated by *McGeehan and Maslowski* (2012) (maxima: 1984, 1990, 1997, minima: 1981, 1988, 1999). The mean volume transport through Lancaster Sound amounts to 0.86 Sv. Other modeling studies obtained volume transports of 0.76 Sv (*McGeehan and Maslowski* (2012), for the years 1979-2004) and 1.02 Sv (*Aksenov et al.* (2010), for the years 1989-2006). The mean liquid freshwater transport simulated by FESOM is 71 mSv, comparing to 48 mSv simulated by *McGeehan and Maslowski* (2012) and 64 mSv simulated by *Aksenov et al.* (2010). Both the simulated volume and freshwater transports are higher than the individual observations (Table 3.2).
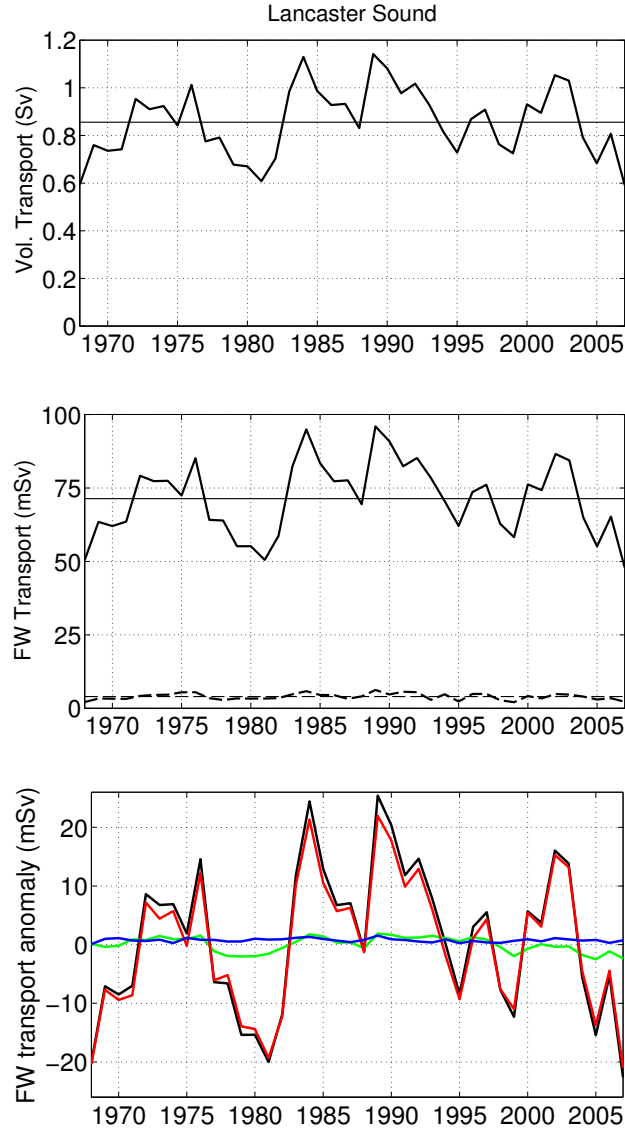
Figure 3.7: Annual mean transports through western Lancaster Sound. Top: Net volume transport. Middle: Liquid (solid line) and solid phase (dashed line) freshwater transports. Thin lines denote mean values for the period 1968-2007. Bottom: Freshwater transport anomaly (black line) and its various contribution: $\int_A \bar{u}\frac{S'}{S_{ref}}dA$ (green line), $\int_A u'\frac{S_{ref}-\bar{S}}{S_{ref}}dA$ (red line) and $\int_A u'\frac{S'}{S_{ref}}dA$ (blue line).

Due to the local fine resolution, the present model simulation allows the quantification of the relative contributions to the transport through the Parry Channel. Time series and means of net volume and freshwater transports into the channel are shown in Table 3.3 and Figure 3.8.

Table 3.3: Mean net transport exiting Lancaster Sound and transports through the gates entering Parry Channel for the time period 1968-2007. Transports into the channel have a positive sign.

	Net volume flux (Sv)	Net FW flux (mSv)
Lancaster	0.86	71
Byam Martin	0.27	22
Penny	0.09	7
McClure	0.45	40
Prince of Wales	0.01	2
McClintock	-0.27	-24
Peel	0.29	26

Net volume transport through McClure Strait accounts for 53% of the total throughflow at western Lancaster Sound, whereas Byam Martin Strait and Penny Strait contribute 32% and 11%, respectively. Volume transports through McClintock Channel and Peel Sound balance each other, and the transport through Prince of Wales Strait is negligible. All transports entering Parry Channel exhibit a similar interannual variability compared to the Lancaster Sound outflow (r=0.88, r=0.94, r=0.96, r=-0.97 and r=0.98, N^* ranging from 11 to 13, significance 99%, for Lancaster Sound transport with transport at Byam Martin Channel, Penny Strait, McClure Strait, McClintock Channel and Peel Sound, respectively). This indicates that transports through the individual channels are driven by the same forcing mechanism.
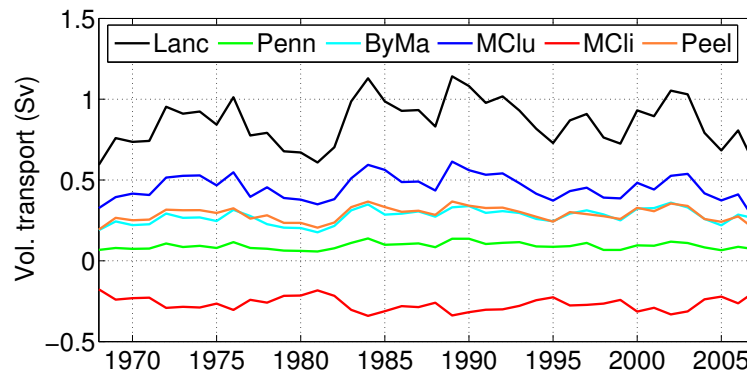
Figure 3.8: Simulated annual mean net volume transports into Parry Channel Positive values mean transports into the channel (Penny Strait: green, Byam Martin Strait: cyan, McClure Strait: blue, McClintock Channel: red, Peel Sound: orange). The transport at the Lancaster Sound (black) is also shown.

3.3.3   Nares Strait

Nares Strait is bordered by landmasses from both sides with Greenland in the east and Ellesmere Island in the west. Time series of annual mean transports through Kennedy Channel (located in the central Nares Strait, with a width of 27.7 km) are depicted in Figure 3.10. In our simulation, Arctic Ocean waters are transported southwards, with almost no northward flow in Nares Strait. The simulated mean volume and freshwater transports of 0.91 Sv and 47.87 mSv are slightly higher than simulated transports by *McGeehan and Maslowski* (2012) (0.77 Sv and 10.38 mSv, respectively) and *Aksenov et al.* (2010) (0.58 Sv and 20 mSv, respectively). The simulated interannual variability matches with the one simulated by *McGeehan and Maslowski* (2012), both showing maxima in volume transport in the years 1984, 1990 and 1997, and minima in the years 1981, 1988 and 1999.

From August 2003 until August 2006 a mooring array was operated in Kennedy Channel as part of the Arctic Sub-Arctic Ocean Flux experiment (*Münchow and Melling*, 2008). Four of the eight deployed moorings provided data during the whole three years. A mean volume transport of 0.57±0.09 Sv was obtained (excluding the top 30 m). The simulated volume transport for
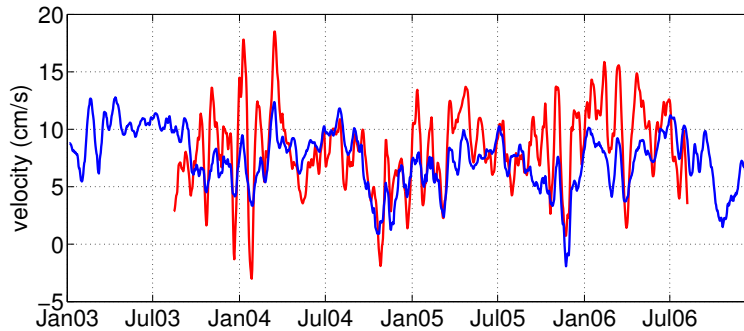
Figure 3.9: Sectionally averaged along channel flow through Kennedy Channel excluding the top 30 m. The red line depicts observations (*Münchow and Melling*, 2008) and the blue line shows the model output as 11-day running means.

this time period amounts to 0.69 Sv, when excluding the top 30 m (0.81 Sv for the whole cross section). Figure 3.9 compares sectionally averaged velocity through the channel obtained from the mooring with simulated velocities and reveals relatively good agreement in magnitude and correlation (r=0.57, N^*=65, significance 99%). The standard deviation of the observed velocity is larger (σ=3.49 cm/s) than the standard deviation of simulated velocity (σ=2.34 cm/s). The lower variability in the model simulation might be linked to the coarse resolution of the atmospheric wind forcing; which should be explored in future studies.
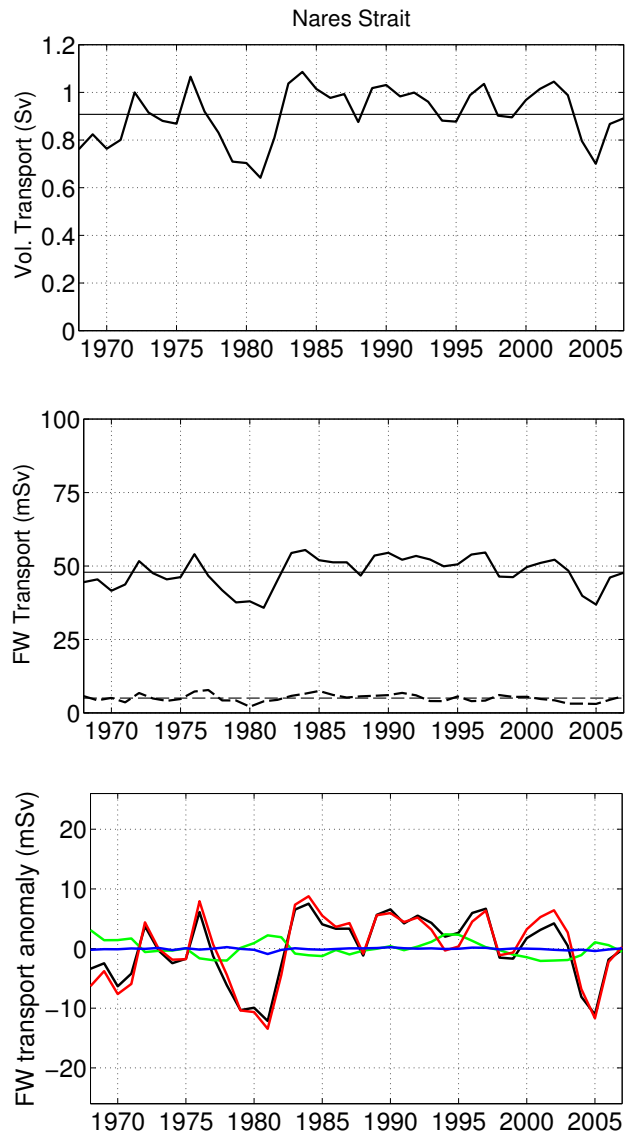
Figure 3.10: The same as Figure 3.7, but for Kennedy Channel, located in the central Nares Strait.

3.3.4 Cardigan Strait and Hell Gate

Waters exiting Jones Sound have to pass the narrow channels of Cardigan Strait and Hell Gate with widths of 8 and 4 km, respectively, hence volume exports through this gate are small compared to Lancaster Sound and Nares Strait (see Table 3.2). With 5 km resolution we cannot resolve these narrow channels, they are widened to have at least one grid point between the solid side walls in order to allow water to pass through. However, the simulated volume transport through Cardigan Strait and Hell Gate is still much lower than the observation. Resolving and studying the flow through these channels is beyond the scope of the current work.

3.3.5 Constituents of the freshwater transport variability

Freshwater transport depends on both the salinity and horizontal velocity fields. In order to determine the constituents of the variability, we split up velocity u and salinity S into its mean (denoted by bar) and its anomaly (denoted by prime), $u = \bar{u} + u'$ and $S = \bar{S} + S'$. Freshwater transport through a cross section A can thus be expressed as the sum of the following four terms: the mean advection of mean salinity, $\int_A \bar{u} \frac{S_{ref} - \bar{S}}{S_{ref}} dA$, the advection of salinity anomalies by the mean currents, $\int_A \bar{u} \frac{S'}{S_{ref}} dA$, the anomalous advection of mean salinity, $\int_A u' \frac{S_{ref} - \bar{S}}{S_{ref}} dA$, and the anomalous advection of salinity anomalies, $\int_A u' \frac{S'}{S_{ref}} dA$. The bottom panels of Figures 3.7 and 3.10 indicate that the freshwater transport anomaly through Lancaster Sound and Nares Strait is determined mainly by the volume transport anomaly. This is in agreement with other modeling studies (*Jahn et al.*, 2009; *Lique et al.*, 2010; *Houssais and Herbaut*, 2011). The correlation between the volume and freshwater transport is r=0.99 (N*=11, significance 99%) and r=0.95 (N*=12, significance 99%) for Lancaster Sound and Nares Strait, respectively.

3.3.6   Overall transports through the CAA

In our simulation, volume transports through Lancaster Sound make up 47% of the total fluxes through the CAA, with Nares Strait and Hell Gate/Cardigan Strait contributing with 50% and 3%, respectively (see Table 3.2). The respective values for net liquid freshwater transports amount to 58%, 39% and 3%. Volume transport through Nares Strait is the largest among the three straits, while Lancaster Sound shows the highest freshwater transport. Larger freshwater transport through Lancaster Sound can be explained by the pathway of Arctic Ocean waters. The western entrance to Parry Channel is closer to the Beaufort Sea and thus to the Beaufort Gyre which is the main freshwater storage of the Arctic Ocean. Nares Strait in contrast, with its northern entrance located in the Lincoln Sea, is farther away from the Beaufort Gyre. Also, due to the larger depth of Nares Strait compared to Lancaster Sound, a higher fraction of saltier LHW enters this strait. Our results are consistent with those described in the work of *Aksenov et al.* (2010): higher freshwater transports through Lancaster Sound than through Nares Strait, because Lancaster Sound is dominated by less salty UHW, and Nares Strait is dominated by the saltier LHW.

Observed net volume transports through the CAA sum up to 1.33 Sv (0.46 Sv for Lancaster Sound, 0.57 Sv for Nares Strait and 0.3 Sv for Cardigan Strait/ Hell Gate, Table 3.2), while Davis Strait volume transport was estimated as 2.6 Sv and 2.3 Sv for two different observational periods (Table 3.1). This discrepancy in the observations can be attributed to different time periods, different instrumentation and the sparseness of instrument coverage across the sections. The simulated net volume transport through the CAA (and through Davis Strait) is 1.81 Sv, and thus lower than observational estimates for Davis Strait throughflow and higher than those for the CAA throughflow. The simulated mean freshwater export of the CAA amounts to 123 mSv, and is slightly higher than the climatological value of 101±10 mSv estimated by *Serreze et al.* (2006).

Simulated freshwater exports in form of sea ice are small compared to liquid freshwater exports. They make up 7% of the liquid freshwater exports

of the CAA in our model. Based on observations, *Peterson et al.* (2012) obtained a similar value for Lancaster Sound: the observed mean solid freshwater transport through this section represents 6% of the observed mean liquid freshwater transport over the period 2003-2007.

Transports through Lancaster Sound and Nares Strait are highly correlated (r=0.86, N*=13, significance 99%, for volume transports, and r=0.80, N*=14, significance 99%, for liquid freshwater transports), indicating related forcing mechanisms for both straits. This will be further discussed in the next section.

3.4   Summary

The CAA is a remote area, covered by sea ice most of the year, and only a limited number of hydrographic observations are available. Therefore, high resolution modeling studies are required in order to better estimate its oceanographic properties and understand the flow dynamics. The present study assesses a new global finite element sea ice-ocean model (FESOM) with high mesh resolution ($\sim$5 km) in the CAA region and intermediate resolution in the Arctic Ocean and northern North Atlantic ($\sim$24 km). FESOM is an unstructured-mesh model, which enables us to refine the mesh locally in areas of interest. This method is particularly useful in the CAA area and allows us to investigate the characteristics of the individual CAA channels. Our study differs from previous coarse resolution Arctic freshwater circulation studies (e.g. *Jahn et al.*, 2009) in the treatment of the CAA bathymetry. While modelers in traditional global ocean models manually widen the CAA straits and sometimes keep only one strait, our resolution of 5 km more realistically represents the geometry of the CAA main straits. The global configuration with local mesh refinement also obviates the need for open boundaries in regional models.

The focus of this study lies on volume and freshwater transports through the CAA and its interannual variability. Mean net volume (liquid freshwater) transports through the CAA's main straits Lancaster Sound and Nares Strait for the time period 1968-2007, as simulated here, amount to 0.86 Sv (71

mSv) and 0.91 Sv (48 mSv), respectively. The simulated variability of volume transport through Lancaster Sound matches well with observations (r=0.81), and also a comparison of sectionally averaged velocity in Nares Strait shows reasonable agreement of the model and observations (r=0.57). The variability of freshwater transport through the CAA is mainly determined by the variability of volume transport as shown by observations (*Peterson et al.*, 2012) and previous model studies (*Jahn et al.*, 2009; *Houssais and Herbaut*, 2011). The total simulated CAA mean freshwater transport is 123 mSv, slightly higher than the estimate (101±10 mSv) of *Serreze et al.* (2006).

The high mesh resolution allows us to quantify the individual contributions to the Parry Channel inflow. 53% of the total throughflow enters the channel through McClure Strait, while 32% and 11% are contributed by Byam Martin Strait and Penny Channel, respectively. Transports through the straits feeding the Parry Channel throughflow show a similar interannual variability, which is due to the same driving mechanism.

Chapter 4

Interannual variability of freshwater transports through the CAA and driving mechanisms

In this section the mechanisms driving the freshwater transport variability through the archipelago will be discussed, with focus on the interannual variability. We concentrate on the liquid component of freshwater, which dominates the total simulated export (93% of the CAA freshwater export is liquid freshwater, see Section 3.3.6).

4.1 The role of sea surface height

The SSH difference between the Arctic Ocean and Baffin Bay (Figure 3.5b) not only leads to a net outflow from the Arctic Ocean, its variability also drives the variation of the CAA throughflow. The correlation of annual mean freshwater transports though Lancaster Sound and Nares Strait with the along strait SSH gradients is significant (Figure 4.1). At Lancaster Sound, the upstream SSH variation plays the major role, and in particular SSH variation on the western side of the strait. There is no significant correlation

of transport with downstream SSH. On the contrary, in Nares Strait it is
rather the downstream SSH and in particular the eastern side that correlates
with transports most significantly. *Houssais and Herbaut* (2011) have also
found that the transport through the CAA is highly correlated with the
along strait SSH gradient for both straits. However, in their case the volume
transport through Lancaster Sound is not so strongly correlated with the
upstream SSH as in our case. They only found high correlation with the along
strait SSH gradient rather than SSH at one single side. Regarding Nares
Strait they observed a high correlation of transport with the downstream
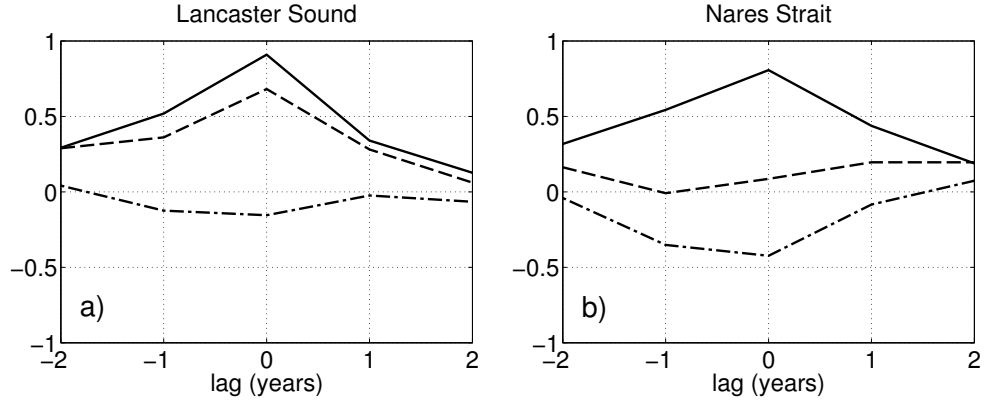SSH, which is similar to our results.

Figure 4.1: Cross correlation of the anomalies of annual mean FW transport
through (a) western Lancaster Sound and (b) Nares Strait with annual mean
SSH upstream (dashed line), downstream (dashed-dotted line) and their dif-
ference (solid line). SSH was calculated as the average over the red boxes
shown in Figure 3.5b.

To quantify the amount of freshwater transported through the CAA ex-
plained by a certain SSH difference, we perform a linear regression analysis.
The time series of annual mean freshwater (and volume) transport $TS_{transport}$
is regressed on the along strait SSH difference $TS_{\Delta SSH}$ by solving the equa-
tion

$$TS_{transport}(i) = a \cdot TS_{\Delta SSH}(i) + b + \epsilon(i), \; i = 1, .., N \qquad (4.1)$$

in a least squares sense, with N being the size of the time series, pa-

rameters a, b and residuum ϵ to be solved. Following the regression analysis we found that an increase of 20 cm in the SSH difference between McClure Strait and Lancaster Sound would result in an increase in freshwater (volume) transport of 138 mSv (1.6 Sv). In Nares Strait an increase of 20 cm would lead to an increase in freshwater (volume) transport of 105 mSv (2.2 Sv).

The spatial maps of correlations between SSH and freshwater transports through Lancaster Sound and Nares Strait reveal more details (Figure 4.2). For both straits a positive correlation is apparent along the Beaufort Sea coast. SSH and transports are negatively correlated in eastern Baffin Bay and in the Labrador Sea. The correlation maps for both straits in Figure 4.2 are very similar, as expected from the fact that transports through both straits are highly correlated. It is then expected that the same large scale atmospheric circulation pattern is responsible for the transport variability through the two straits, which increases (decreases) the SSH along the American coast in the Arctic Ocean and decreases (increases) the SSH in the Labrador Sea and Baffin Bay at the same time. This will be further discussed in the following sections.
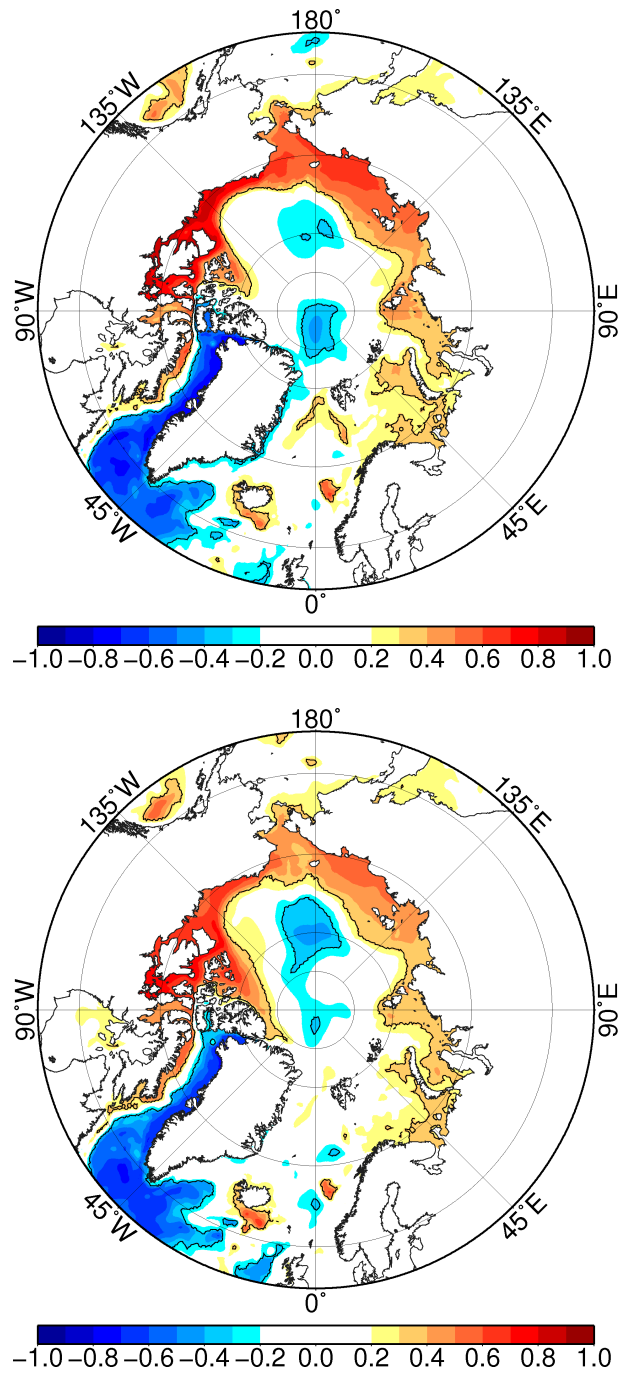
Figure 4.2: Correlation of the simulated annual mean FW transport through Lancaster Sound (left) and Nares Strait (right) with annual mean sea surface height. Black contours indicate areas of 95% significance.

4.2   Large scale atmospheric forcing

As seen in the previous section there is an indication that there could exist a large scale forcing mechanism which simultaneously leads to a change of SSH in the Arctic and in the Labrador Sea/Baffin Bay. By investigating the relationship of CAA transports with sea level pressure, we observe that transports through both straits are negatively correlated with sea level pressure in the Arctic Ocean and around Greenland, and are positively correlated in the northern North Atlantic (Figure 4.3).

The correlation pattern are similar for both straits. This dipole structure is related to the North Atlantic Oscillation (NAO), the dominant mode of atmospheric variability in the North Atlantic and Arctic Ocean (*Dickson et al.*, 2000). A high NAO-index is characterized by a low pressure anomaly in the Arctic and around Greenland, and by a high pressure anomaly in the central North Atlantic. A low pressure anomaly in the Arctic drives a cyclonic wind anomaly, whereas a strong pressure difference between the two anomaly cells leads to strong winds over the Labrador Sea. The FW transports through Lancaster Sound and Nares Strait are highly correlated with each other, and both are correlated with the NAO index (Figure 4.4). The correlation coefficients between the NAO index and the FW transports are r=0.68 (N^*=11, significance 97%) and r=0.52 (N^*=12, significance 90%) for Lancaster Sound and Nares Strait, respectively.

This is consistent with the study by *Condron et al.* (2009) who described experiments with artificial forcing consisting of extremely negative and positive NAO phases, and observed an acceleration of Arctic Ocean freshwater exports, also through the CAA, during the positive NAO phase. Apparently the same large scale atmospheric pattern controls the transport through both CAA straits. In section 4.1 we demonstrated that transport through Lancaster Sound can be explained by SSH changes in the Arctic Ocean, whereas Nares strait transport is more linked to SSH changes in Baffin Bay. In the following we will explain the changes in SSH upstream and downstream of the CAA with the variability of the large scale atmospheric forcing.
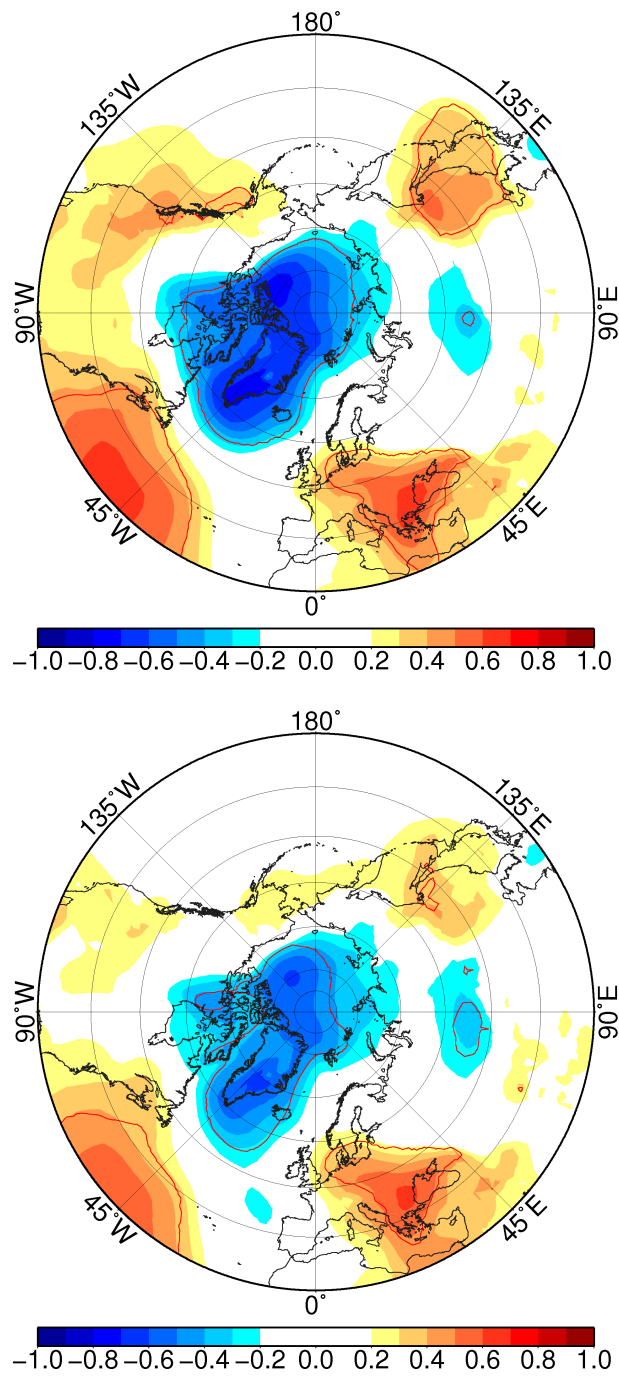
Figure 4.3: Correlation of annual mean freshwater transport through western Lancaster Sound (left) and Nares Strait (right) with annual mean sea level pressure. Red contours indicate areas of 95% significance.
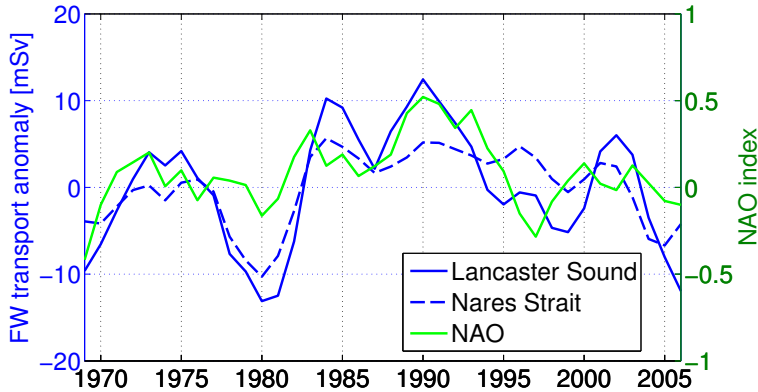
Figure 4.4: The index of the North Atlantic Oscillation (green) and anomalies of net freshwater transports through Lancaster Sound (blue line) and Nares Strait (dashed blue line). Time-series are 3 year-running means. The NAO index was provided by NOAA Climate Prediction Center at their web site http://www.cpc.ncep.noaa.gov/products/precip/CWlink/ENSO/verf/new.-nao.shtml.

4.3 Arctic Ocean forcing on Lancaster Sound throughflow

Figure 4.1 shows that Lancaster Sound transport is highly correlated with sea level changes upstream. In the last section we pointed out that high transports through Lancaster Sound are connected with a low pressure anomaly in the Arctic Ocean, which is associated with a cyclonic wind anomaly. In the following the impact of winds will be further investigated by applying a multiple linear regression analysis. At every node of the surface mesh the time series of the annual mean FW transport was regressed on the annual mean surface wind for time period 1968-2007. We write the dependent variable, the simulated FW transport T_{fw}, as a linear combination of the parameters a, b and c:

$$T_{fw_i} = a\,u_i + b\,v_i + c + \epsilon_i, \; i = 1,...,N, \qquad (4.2)$$

with u_i and v_i being the independent variables, observed zonal and merid-

ional wind components from the CORE-II data set, respectively, ϵ being an error term, and N denoting the number of data points in time. The coefficients a, b and c are found for each grid point by minimizing the residual term in a least square sense. Figure 4.5 depicts the correlation coefficient of modeled and predicted data values, i.e. of T_{fw} and $a \cdot u + b \cdot v$, and arrows indicate the normalized optimal wind direction $(a,\, b) \cdot \frac{1}{\sqrt{a^2+b^2}}$. The Lancaster Sound freshwater transport has the highest correlation with wind west of Banks Island in the Beaufort Sea (the maximum correlation is r=0.73, at -118.8°E, 72.8°N). This corresponds to northeastward winds. Our result is consistent with *Peterson et al.* (2012) who performed a similar analysis with Lancaster Sound volume transports derived from observations for the period of 1998-2011 and had a similar finding. Figure 4.5 reveals that a positive (negative) freshwater transport anomaly through Lancaster Sound corresponds to a cyclonic (anticyclonic) wind anomaly pattern in the Beaufort Sea.
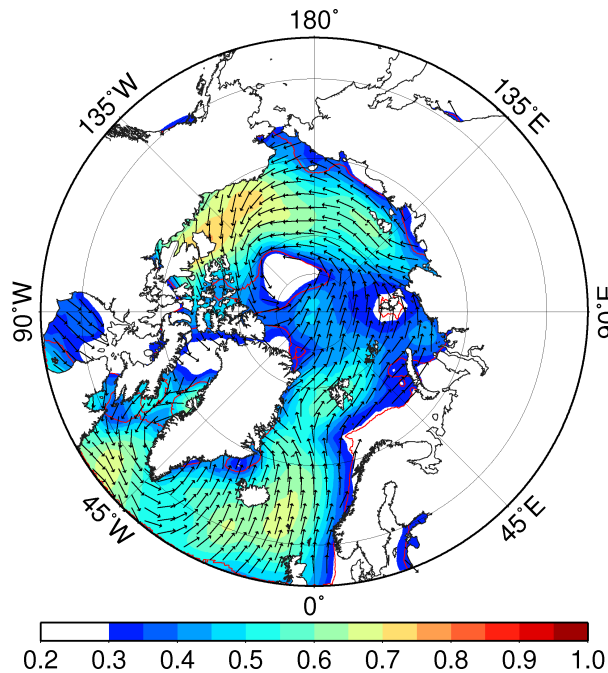

Figure 4.5: Correlation of the simulated annual mean freshwater transport through western Lancaster Sound with the annual mean wind field at 10 m height. Arrows denote the corresponding optimal wind direction. Red contours indicate areas of 95% significance.

Proshutinsky et al. (2002) demonstrated that the Beaufort Gyre, the main freshwater storage of the Arctic Ocean, accumulates freshwater during an anticyclonic wind regime and releases freshwater during a cyclonic regime. An anticyclonic wind regime in the Beaufort Sea leads to accumulation of water masses in the gyre and thus raised SSH in the center of the gyre, whereas a cyclonic regime leads to divergence of Beaufort Gyre surface water and raised SSH along the American coast. Therefore, it is the wind regime over the western Arctic Ocean that drives the variability of SSH along the American coast, thus the variability of FW transport through the Lancaster Sound. And the wind regime is strongly linked to the large scale atmospheric forcing (Figure 4.3).

4.4   Sea level in Baffin Bay and Nares Strait throughflow

In Section 4.1 we showed that the transport through Nares Strait is correlated with sea level in eastern Baffin Bay (Figure 4.1). The correlation of Nares Strait transport with sea level pressure (Figure 4.3) reveals that high transports are associated with a low pressure anomaly over Greenland and a high pressure anomaly at around 30° latitude. This entails intensifying storms over the northern North Atlantic, cooling in the Labrador Sea, a stronger cyclonic circulation south of Greenland (subpolar gyre) and a decrease of SSH in this area (*Lohmann et al.*, 2008). This is also apparent when correlating the simulated annual mean freshwater transport through Nares Strait with the surface heat flux (Figure 4.6), which reveals a high negative correlation in the Labrador Sea, more precisely in the area which is ice free in the winter.

The analysis of simulated SSH time series in several locations in the eastern Baffin Bay (green boxes in Figure 4.6) shows that there is no time lag in SSH between the three locations, neither on daily, monthly nor annual time scales (Figure 4.7). This indicates that it is not the advection of low density waters within the West Greenland Current, but fast wave propagation that leads to low sea level along the West Greenland coast.
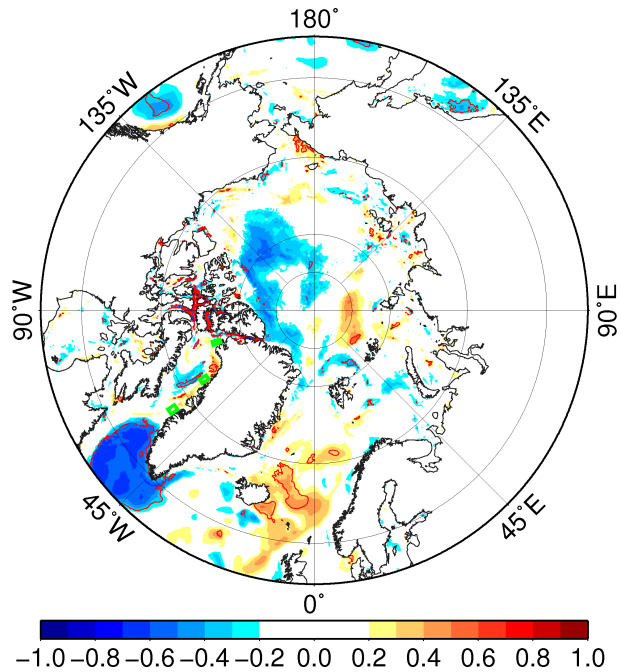
Figure 4.6: Correlation of annual mean freshwater transport through Nares Strait with surface heat flux (downward positive). Green boxes are taken for the computation of sea surface height indices. Red contours indicate areas of 95% significance.

This explanation of SSH variability in the eastern Baffin Bay is similar to the one by *Houssais and Herbaut* (2011). They also draw the conclusion that during a NAO-positive phase the cooling in the Labrador Sea leads to lower SSH there, which then propagates northwards into eastern Baffin Bay as fast waves. Another hypothesis was proposed by *McGeehan and Maslowski* (2012). They have only considered the seasonal signal and suggested that it is the volume flux of the West Greenland Current that drives the SSH in eastern Baffin Bay. However, the instantaneous response of the SSH at Smith Sound to Labrador Sea SSH suggests that slow advection processes, while undeniably present on the seasonal scale, cannot explain the SSH variability at Smith Sound in our simulation.
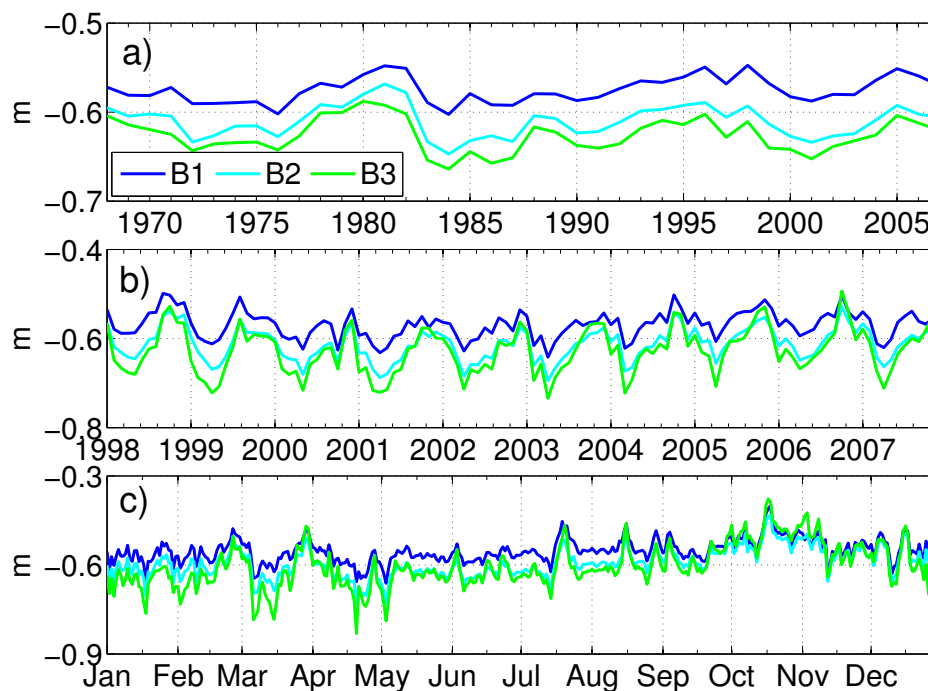
Figure 4.7: Time series of (a) annual, (b) monthly and (c) daily (for 2006) sea surface height averaged over the green boxes in Figure 4.6. B1 is the northernmost box and B3 the southernmost box.

4.5 Summary

A statistical analysis has been performed to explain the interannual variability of liquid freshwater transports through Lancaster Sound and Nares Strait. The main driver of transports is the along strait SSH difference, with Lancaster Sound transport being mainly driven by the upstream SSH variation and Nares Strait mainly by the downstream SSH variation. The varying sea level upstream of Lancaster Sound can be explained by the change in the large scale wind regime in the Arctic Ocean, whereas the varying SSH in northern Baffin Bay can be explained by ocean-atmosphere heat exchanges over the Labrador Sea.

The variability of the CAA transports is related to the NAO, the dominant large scale atmospheric pressure pattern in the North Atlantic. Re-

sponses to the positive and negative phases of the NAO can be observed both in the Beaufort Sea and in Baffin Bay. In the positive NAO phase, the atmospheric circulation over the western Arctic Ocean is mainly in the cyclonic phase (see e.g. *Proshutinsky et al.*, 2002), leading to a loss in the freshwater storage in the Beaufort Gyre and an increase in SSH along the American coast, and thus increased FW transport through Lancaster Sound. In the Labrador Sea the strong cooling during the NAO positive phase results in low SSH, which is propagated through fast waves northwards to Smith Sound leading to higher transports through Nares Strait.

Chapter 5

Impact of mesh resolution in the CAA on the Atlantic Ocean circulation

5.1 Motivation

The Arctic Ocean is strongly stratified due to large surface freshwater input from river runoff, excess of precipitation over evaporation and Bering Strait inflow (*Serreze et al.*, 2006). Arctic freshwater is exported through the narrow straits of the Canadian Arctic Archipelago (CAA) and through the relatively deep and wide Fram Strait into the North Atlantic. Freshwater exported from the Arctic Ocean may have a significant impact on the Atlantic Meridional Overturning Circulation (AMOC, see *Goosse et al.*, 1997; *Wadley and Bigg*, 2002; *Cheng and Rhines*, 2004; *Komuro and Hasumi*, 2005). It is plausible, therefore, that an adequate representation of Arctic freshwater export in climate models is crucial when it comes to predicting climate variability and change.

Despite the importance of the freshwater export through the Arctic gateways its monitoring and numerical simulation has been a challenge, especially for the CAA. In situ measurements of the ocean hydrography and velocity in the narrow straits of the CAA are still rather sparse in time and space due

to their remote location and harsh weather conditions (*Prinsenberg et al.*, 2009; *Münchow and Melling*, 2008). Parry Channel and Nares Strait in the CAA, for example, have a minimum width of about 52 km and 28 km, respectively. In traditional climate models these straits are too narrow to be explicitly resolved, and in practice they are manually widened in order to to allow for some freshwater export. Most of our understanding of oceanic key processes in the CAA is based on high-resolution *regional* models (e.g. *Wang et al.*, 2012a; *McGeehan and Maslowski*, 2012) given past and present computational limitations. *Global* high-resolution modeling studies are upcoming, e.g. by *Aksenov et al.* (2010), but cover shorter time periods so far. Besides, the study by *Jahn et al.* (2012) shows a large spread of the state-of-the-art models in simulating the Arctic Ocean freshwater exports, with better model-to-model agreement in the CAA than in Fram Strait.

A new generation of global models is emerging which employ multi-resolution mesh methods, such as finite elements, and therefore allow local refinement without the necessity for nesting. The availability of such models opens up new horizons for both dynamical downscaling and upscaling. The main motivation for developing multi-scale climate models is based on the following two hypotheses: The representation of local dynamics can be improved in a global set-up (downscaling); and a better representation of small-scale processes leads to a better simulation of the large scale circulation (upscaling). To test these hypotheses, it is necessary to identify dynamically important regions where meso-scale processes and hence local mesh refinement are believed to be important. The geometrical properties of the CAA (small-scale aspects) and its proximity to the deep convection sites (with potential climate relevance) make it a very promising testbed.

In this work FESOM is used with and without mesh refinement in the CAA in order to establish the role of resolution for representing the freshwater transport through the CAA and to understand possible impacts on the large-scale ocean circulation. This is one of the first studies to test the above-mentioned hypothesis for one special case —the CAA.

Two experiments (denoted by HIGH and LOW) were performed, with the only difference in the configuration being the mesh resolution in the CAA

area. In experiments HIGH and LOW, the mesh resolution in the CAA is 5 km and 24 km, respectively. North of 50°N the resolution in both experiments is 24 km, and in the global oceans it is 1.5° (see Section 2.5, Figure 2.2 and Table 2.2). Figure 5.1 depicts the global mesh used in experiment HIGH.
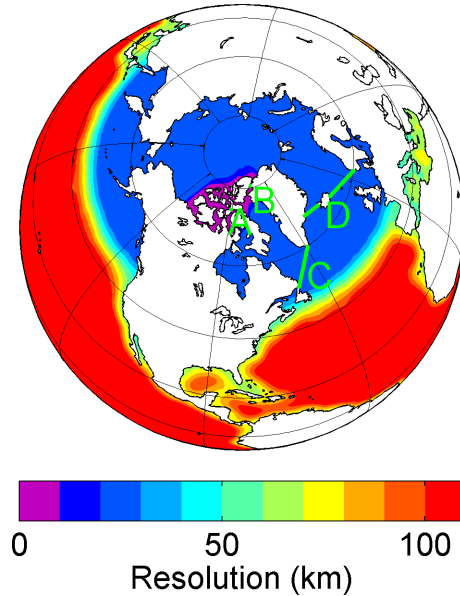

Figure 5.1: Northern hemisphere view of the global mesh used for experiment HIGH. The color patch shows the mesh resolution. The CAA region has a resolution of 5 km. Green lines indicate Lancaster Sound (A), Nares Strait (B), a section near 53°N (C) and the Greenland-Iceland-Norway section (D).

5.2 Freshwater transport through the CAA

Time series of liquid freshwater transports (relative to a salinity of 34.8 psu, the mean salinity of the Arctic Ocean) through the two main straits of the CAA are shown in Figure 5.2a,b. The freshwater export rates are higher for both straits in HIGH than they are in LOW. In Lancaster Sound the mean liquid freshwater transport amounts to 33 mSv and 71 mSv in LOW and HIGH, respectively, while in Nares Strait it is 26 mSv and 48 mSv. Importantly, the total liquid freshwater transport through the CAA in HIGH (119 mSv) is much closer to the climatological liquid freshwater transport

(101 mSv) estimated by *Serreze et al.* (2006). Freshwater transports in form of sea ice through the CAA account only for 7% of the total freshwater transports (9 mSv and 2 mSv in cases HIGH and LOW, respectively).
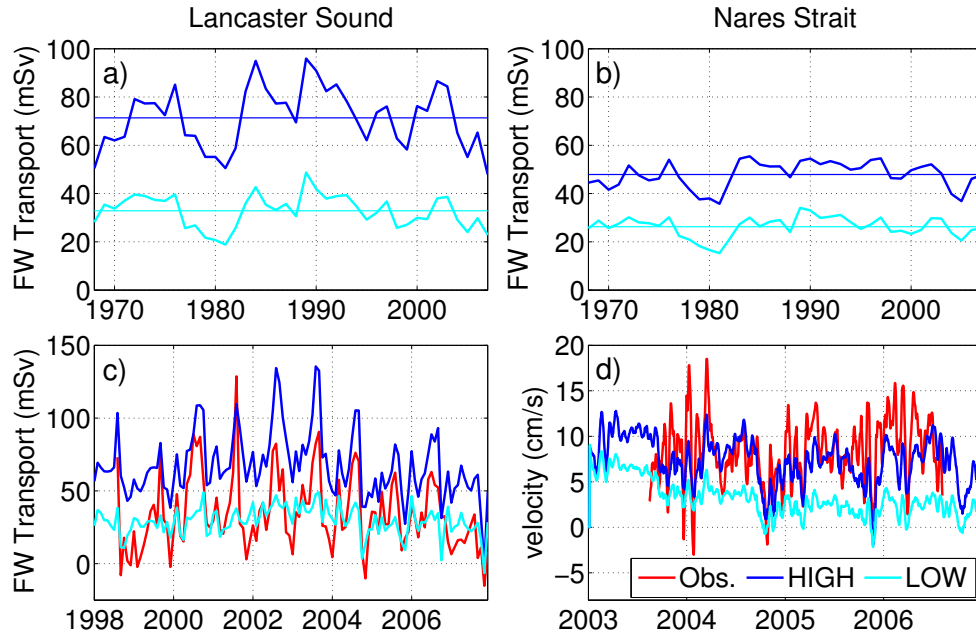

Figure 5.2: (a) Annual mean net liquid freshwater transport through Lancaster Sound. Horizontal lines denote the mean value for 1968-2007. (b) Same as (a) but for Nares Strait. (c) Monthly mean net liquid freshwater transport through Lancaster Sound for experiments HIGH, LOW and observation (red, *Peterson et al.*, 2012). (d) 11-day running mean of sectional velocity in Nares Strait excluding the top 30 m. The running mean is shown to better illustrate the low frequency variability which is the focus of the current work. The red line depicts the observation (*Münchow and Melling*, 2008). In all four plots, results from experiments HIGH and LOW are depicted by blue and cyan lines, respectively. Freshwater transports are calculated relative to 34.8 psu and southward transports have a positive sign.

Mooring arrays have been deployed in the western Lancaster Sound since 1998 to monitor the volume and freshwater transport (*Prinsenberg et al.*, 2009; *Peterson et al.*, 2012). The observed and simulated monthly mean freshwater transports in Lancaster Sound are shown in Figure 5.2c. Evidently, there is a good correlation between the observed time series with the

one obtained by HIGH (r=0.82); considerably lower correlations are found for LOW (r=0.62). Furthermore, HIGH also shows improvements on the level of freshwater export variability as indicated by the standard deviation of the monthly mean data (observations: $\sigma = 25\,\mathrm{mSv}$, HIGH: $\sigma = 23\,\mathrm{mSv}$, LOW: $\sigma = 10\,\mathrm{mSv}$). On the other hand, its mean value for this period ($68\,\mathrm{mSv}$) is too high compared to the estimates obtained from the observations ($34\,\mathrm{mSv}$). A pronounced overestimation of the Lancaster Sound transport compared to the same observational dataset was also reported in a regional high resolution model (*Lu et al.*, 2010). It is possible that this overestimation is due to more general model deficiencies which are not directly related to model resolution. It is also conceivable that model validation is hampered by large observational uncertainties given that the results presented here were derived from only two (some periods four) moorings which generally did not observe the uppermost $30\,\mathrm{m}$, which contains most of the freshwater. This might leave the observational estimate sensitive to the methods used for interpolation in the horizontal and extrapolation in the vertical (*Peterson et al.*, 2012), respectively.

From August 2003 to August 2006 a mooring array was operated in Kennedy Channel in Nares Strait (*Münchow and Melling*, 2008). Considering the fact that the upper $30\,\mathrm{m}$ depth was missing in the observation, *Münchow and Melling* (2008) only provided the total volume transport below $30\,\mathrm{m}$ depth for Nares Strait ($0.57 \pm 0.09\,\mathrm{Sv}$). Corresponding volume transports simulated by FESOM for the same time period amount to $0.69\,\mathrm{Sv}$ and $0.25\,\mathrm{Sv}$ in runs HIGH and LOW, respectively. Figure 5.2d compares the sectionally averaged velocity in Kennedy Channel from the mooring array and simulations. The experiments HIGH and LOW have similar correlations with the observation (r = 0.57 and 0.49, respectively); the mean value of HIGH, however, is much closer to the observed value.

There is a large discrepancy in the observations of CAA and Davis Strait transports. The observed Davis Strait volume transport is 2.3 - 2.6 Sv (*Curry et al.*, 2011; *Cuny et al.*, 2005), while the observed CAA volume transport is only 1.33 Sv (0.46 Sv for Lancaster Sound estimated by *Peterson et al.* (2012), 0.57 Sv for Nares Strait estimated by *Münchow and Melling* (2008) and 0.3

Sv for Hell Gate and Cardigan Strait estimated by *Melling et al.* (2008)). This discrepancy is also found in the freshwater transports. The simulated Davis Strait freshwater transport of HIGH (111 mSv) is much closer to the observational estimate (ranging between 92 and 116 mSv according to *Curry et al.* (2011) and *Cuny et al.* (2005)) than the value of LOW (65 mSv).

Despite noticeable differences, the freshwater transports in the two simulations are highly correlated (r = 0.85 for Lancaster Sound and r = 0.79 for Nares Strait). The interannual variability of freshwater transport through the CAA is correlated with the variability of the along strait sea surface height difference, which is in turn driven by local forcing associated with the large scale atmospheric circulation (*Houssais and Herbaut*, 2011). This may explain why the correlation for LOW is relatively high, despite its relatively poor representation of the CAA.

As discussed above, the liquid freshwater export through the CAA is enhanced by 64 mSv when horizontal resolution is increased from about 24 to 5 km. This increase is accompanied by a decrease of freshwater export through Fram Strait by 20 mSv; this indicates that the near-surface Arctic freshwater content becomes lower in the case HIGH (most pronounced in the Lincoln Sea and north of Greenland, see Figure 5.3). An observational estimate of the Fram Strait freshwater export for 1998-2008 is 66 mSv (relative to a reference salinity of 34.9 psu, contributions to the transport over the continental shelf are estimated by simulations, *de Steur et al.*, 2009). Considering the same reference salinity, the value of HIGH for 1998-2007 (60 mSv) matches better with observations than the value of LOW (81 mSv). From idealized model simulations employing the Island Rule for the flow around Greenland it follows that the circulation east and west of Greenland balances each other and that the individual contributions depend on friction and winds (*Joyce and Proshutinsky*, 2007). In the next section we will show that the changed distribution and amount of freshwater export on the two sides of Greenland leads to changes in the large-scale circulation of the North Atlantic.
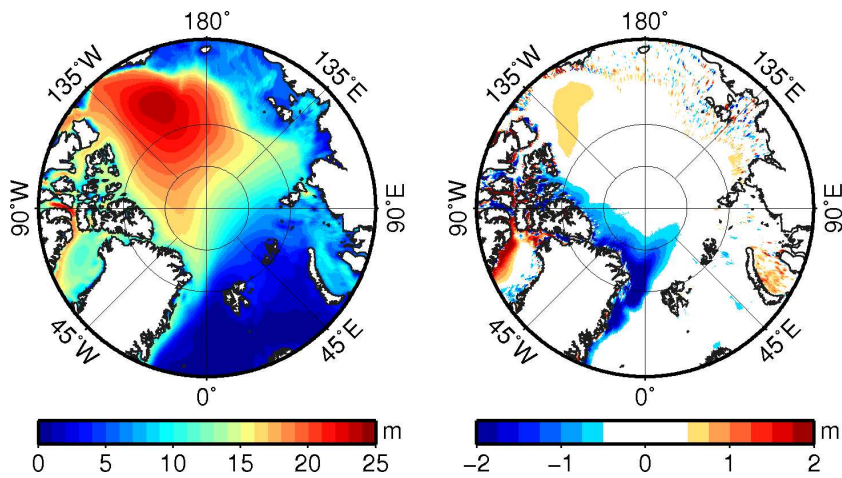
Figure 5.3: Mean liquid freshwater content integrated from 500 m depth to the surface relative to 34.8 psu for 1968-2007 for experiment LOW (left) and its difference from experiment HIGH (HIGH minus LOW, right).

5.3 Large scale circulation

Figures 5.4a and b show the mean AMOC streamfunction in experiment LOW and the difference between HIGH and LOW, respectively. The strength of the intermediate overturning cell increases over the whole Atlantic when the CAA region is better resolved. The largest increase in the North Atlantic amounts to about 2 Sv. The sizable change in the large-scale ocean circulation highlights the importance of adequately resolving the details of the freshwater export from the Arctic in climate simulations.

The North Atlantic Deep Water (NADW), which feeds the intermediate cell of the AMOC, is exported from the Labrador Sea by the Deep Western Boundary Current (DWBC). The DWBC has primarily a thermohaline origin through the processes of deep convection and water-mass ventilation in the GIN (Greenland-Iceland-Norwegian) Seas and in the Labrador Sea (*Böning et al.*, 2006; *Schweckendiek and Willebrand*, 2005). Previous studies indicate that both regions have significant impact on the overturning circulation (*Latif et al.*, 2006; *Schweckendiek and Willebrand*, 2005; *Danabasoglu et al.*, 2012; *Eden and Jung*, 2001).
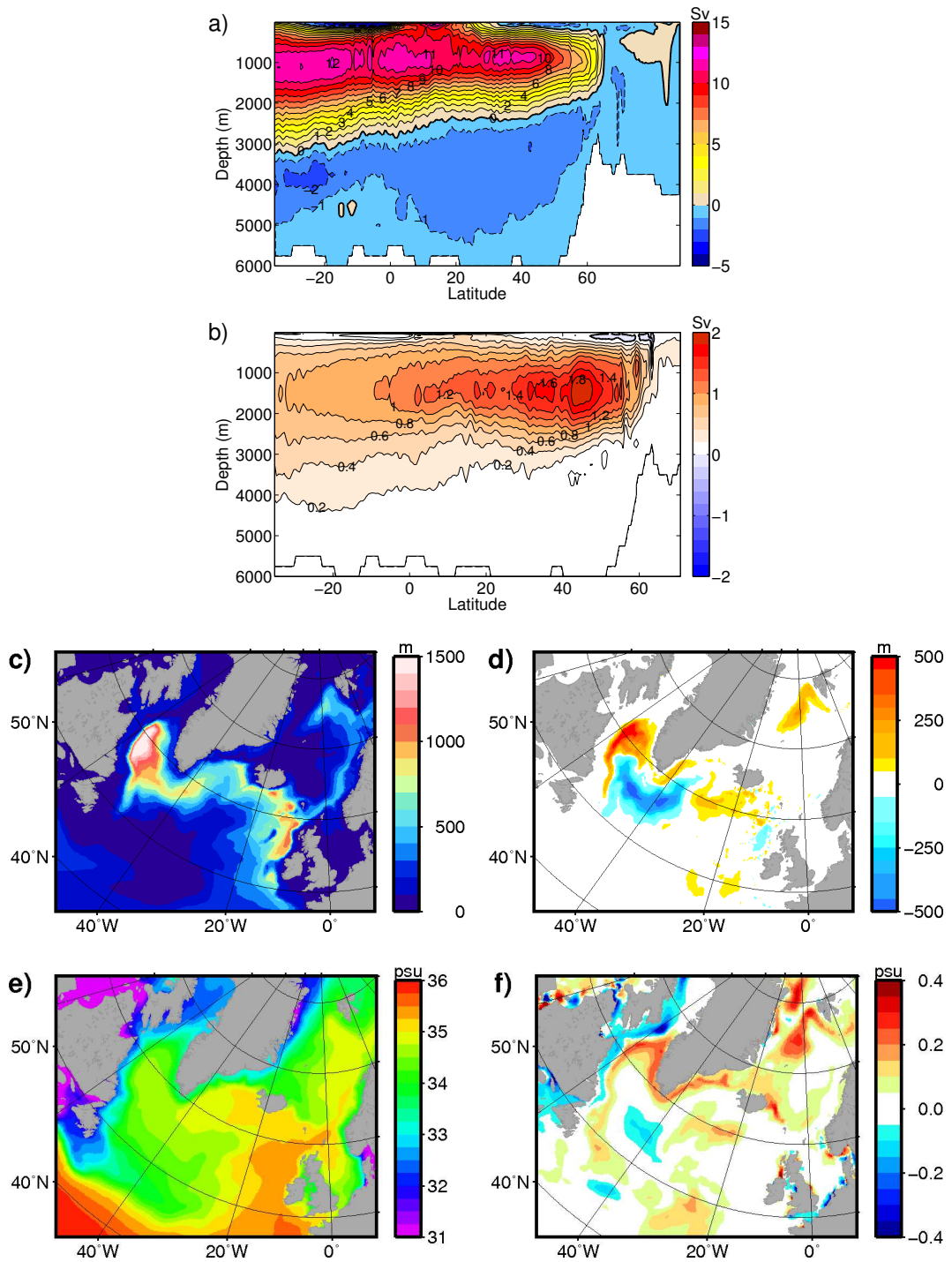
Figure 5.4: (a) Mean AMOC streamfunction for the time period 1968-2007 for experiment LOW and (b) its difference from experiment HIGH (HIGH minus LOW). (c) Mean winter (January-March) mixed layer depth for 1968-2007 for experiment LOW and (d) its difference from experiment HIGH (HIGH minus LOW). (e) Mean salinity from the surface to 50 m depth for 1968-2007 for experiment LOW and (f) its difference from experiment HIGH (HIGH minus LOW).

During wintertime mixed layer depth (MLD) represents a measure of the convection intensity. Figures 5.4c and d show the winter mean MLD in run LOW along with the difference between HIGH and LOW. Deep MLD are observed in the Labrador Sea, south of the Greenland-Iceland-Scotland Ridge, with intermediate depths in the GIN Seas; this is in agreement with observations (*de Boyer Montégut et al.*, 2004). When the CAA region is better resolved, the MLD increases significantly in the northern Labrador Sea (from $1,480$ m in run LOW to $1,670$ m in HIGH for the 40 years mean maximum); on the other hand, it reaches to lower depths south of Greenland. Moderate increases in MLD are found in the northern GIN seas.

The changes in the MLD can be explained by changes in the Arctic freshwater pathways (see Figure 1.2 for the circulation pattern in Baffin Bay and the Labrador Sea). The freshwater exported through Fram Strait flows southward along the east Greenland coast as part of the East Greenland Current (EGC). When the CAA region is better resolved, allowing for more export, the freshwater transport in the EGC is reduced. This slightly weakens the stratification along the ice edge in the Greenland Sea, thus intensifying the convection slightly as shown by the increased MLD. As shown in Figure 5.5a, overflow export from the GIN Seas is only marginally affected.

The EGC feeds the West Greenland Current (WGC) after passing the southern tip of Greenland. A reduction in the freshwater transport in the EGC decreased the WGC and hence the freshwater input to the Labrador Sea (changes in the salinity of the top 50 m are shown in Figure 3f). This explains the enhanced convection in the northern Labrador Sea in HIGH (Figure 5.4d). Although the freshwater export through the CAA increases in case HIGH, it propagates southward along the shelf and does not penetrate the northern Labrador Sea as that from the WGC does (*Myers*, 2005; *Myers et al.*, 2009). Part of the anomalous freshwater from the CAA in case HIGH recirculates in the North Atlantic subpolar gyre (SPG) and increases the stratification south of Greenland, leading to weaker convection there.
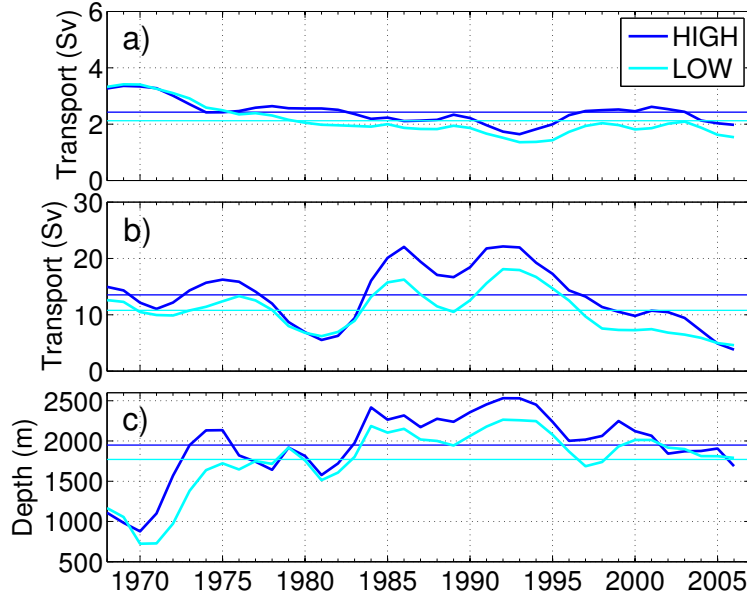
Figure 5.5: (a) Overflow (defined by $\sigma_0 \geq 27.8$) export rate from the GIN Seas (section D in Figure 5.1). (b) Dense portion ($\sigma_0 \geq 27.7$) of the DWBC transport near 53°N (section C in Figure 5.1). (c) Maximum winter (January-March) mixed layer depth in the box 60°-50°W and 55°-62°N. All time series are 3-year filtered. Horizontal lines denote the mean value for 1968-2007.

As the convection and water-mass ventilation in this region is less significant than in the Labrador Sea's interior, the resulting DWBC transport at the southwestern Labrador Sea (near 53°N) is higher in HIGH (Figure 5.5b). This explains the enhanced strength of the AMOC (Figure 5.4b).

Figure 5.5c shows the time series of the maximum winter mean MLD in the Labrador Sea. As expected, this proxy for open ocean convection correlates well with the DWBC transport (r = 0.56 (0.55) for time lags of 0 (1) year in case of HIGH, with convection leading for positive lags). Both simulations capture the reduced convection in the early 1970s associated with the Great Salinity Anomaly (*Lazier*, 1980) and the strong convection events in the mid-1970s, mid-1980s, and early 1990s (*Lazier et al.*, 2002; *Böning et al.*, 2006). The fact that LOW reproduces the decadal variability of DWBC and AMOC is consistent with the notion that it is primarily linked to the atmospheric circulation associated with the North Atlantic Oscillation

(e.g., *Curry et al.*, 1998; *Lazier et al.*, 2002; *Eden and Jung*, 2001).

5.4 Summary and conclusion

In this work the multi-resolution model FESOM is used to study the freshwater export through the CAA and its impact on the large scale ocean circulation. By using a multi-resolution approach it becomes possible to realistically represent the narrow straits of the CAA in a global model. A comparison with observations reveals that the numerical representation of the freshwater transport through the CAA benefits from the use of a locally refined mesh. Increased mesh resolution in the CAA region not only allows for more freshwater to exit the Arctic through the CAA, it also improves the representation of interannual freshwater export variability.

Better resolving the CAA region leads to a redirection of Arctic Ocean freshwater transports, with more export through the CAA and less export through Fram Strait. This redirection has significant effects on the stratification of the near surface waters in the Labrador Sea and thus open ocean convective activity. One possible explanation for this finding is that freshwater from the EGC and WGC more vigorously penetrates into the interior of the Labrador Sea than that from the Baffin Island and Labrador Currents (*Myers*, 2005; *Komuro and Hasumi*, 2005). The total Arctic freshwater export to the North Atlantic is higher when the CAA region is more adequately resolved. Part of the increased freshwater enters the subpolar gyre and increases the stratification south of Greenland. Overall, however, ventilation and DWBC is intensified, leading to a stronger AMOC.

The high-resolution regional modeling study by *McGeehan and Maslowski* (2011) shows that mesoscale eddies may play an important role in transporting freshwater from the western Labrador Sea into its interior. In this paper we only increased the model resolution locally in the CAA, leaving horizontal resolution in the Labrador Sea region relatively coarse (24 km). Future work aims to increase model resolution simultaneously in both the CAA and the deep convection regions to more comprehensively assess the role of Arctic freshwater export in the climate system. The work of *McGeehan and*

Maslowski (2011) also shows that the major shelf to interior liquid fresh-water flux on annual time scales occurs from Hamilton Bank southward, as found from the coarse resolution model study by *Myers* (2005). Therefore, the results in our work are expected to be sensible in general, which needs to be verified in future work.

Using the CAA as a case study we demonstrate that multi-resolution models allow to simultaneously improve the representation of small-scale dynamical processes in a global setup (downscaling) and explicitly account for the influence of meso-scale processes in dynamically active key-regions on the large-scale circulation (upscaling). Our results therefore indicate that multi-resolution models might prove extremely useful when it comes to significantly advancing the field of climate modeling.

Chapter 6

Conclusions and Outlook

The Canadian Archipelago connects the Arctic Ocean with Baffin Bay and is one of the main gateways for Arctic Ocean freshwater to enter the North Atlantic. It is a remote area with harsh weather conditions, and thus only a limited number of hydrographic observations are available. The area is characterized by narrow straits, which are not accurately represented in traditional ocean general circulation models. In this work, we apply a global configuration of FESOM with the Canadian archipelago explicitly highly resolved ($\sim$5 km). The local high resolution allows for studying small-scale processes, while the global set-up enables us to investigate the impact of these small-scale processes on the large-scale circulation. Hindcast simulations were performed for the period 1958-2007, forced by the CORE-II atmospheric reanalysis data. Two model set-ups (high and coarse resolution in the CAA) allow us to investigate the impact of locally refined meshes. The main findings of this work are:

- Assessment of the model in the CAA region revealed a high correlation of modeled and observed transport through Lancaster Sound and averaged velocity in Nares Strait (r=0.81 and r=0.57, respectively). The modeled seasonal cycle of the Lancaster Sound transport matches well with the observed seasonal cycle, indicating that the model realistically represents the CAA ocean dynamics. In fact, as hydrographic observations mostly do not cover the oceanic surface layer (e.g. *Münchow and*

Melling, 2008), our results provide useful information for this missing
region in observations. As the model resolves also the narrow straits of
the CAA, the relative contributions to the transport through the Parry
Channel was quantified.

- The validation of the model in the Arctic Ocean demonstrated that the
  model is capable to realistically simulate ocean and sea ice conditions
  in this region. Sea ice concentration in the northern hemisphere can be
  realistically simulated, although FESOM slightly overestimates sea ice
  concentration in the summer months.

- The interannual variability of freshwater transport through the CAA
  is driven mainly by the sea surface height gradient between the Arctic
  Ocean and Baffin Bay, with Lancaster Sound transport being driven
  by the upstream sea level variation and Nares Strait transport by the
  sea level variation in northeastern Baffin Bay. The variability of fluxes
  through Lancaster Sound and Nares Strait is mainly determined by
  that of the SSH on the shelf along the Beaufort Sea coast and in the
  northeastern Baffin Bay, respectively. Sea level variations north of
  the CAA are explained with changes in the wind regimes (cyclonic vs.
  anticyclonic) associated to release or accumulation of freshwater from
  the Beaufort Gyre, whereas sea level in the northeastern Baffin Bay
  can be attributed to ocean-atmosphere heat fluxes over the Labrador
  Sea. Both processes are linked to the North Atlantic Oscillation type
  of variability.

- Mesh refinement in the CAA region leads to a 'redirection' of freshwa-
  ter pathways, with more freshwater export through the CAA and less
  through Fram Strait. These changed freshwater pathways affect the
  stratification of the near surface layers in the Labrador Sea, and thus
  the convection activity in this region, leading to a stronger AMOC.

Future perspectives   As a next step it should be considered to not only
highly resolve the CAA, but also other important regions of the world oceans.

Especially when studying the impact of Arctic Ocean freshwater exports on the deep water formation in the North Atlantic, areas with strong convection activity like the Labrador Sea and Greenland Seas as well as overflow areas like the Denmark Strait should be better resolved simultaneously.

The ice conditions in Nares Strait are characterized by ice bridges, which form frequently in its northern part. The FESOM ice component is not able to simulate these ice bridges accurately. Further developing the sea ice model remains a task in the future work.

Tides play an important role in the Canadian archipelago, especially in mixing colder surface waters with warmer bottom waters. This has an impact on the formation of polynyas which form frequently in the archipelago region (*Hannah et al.*, 2009). Hence, it should be considered to incorporate tides into the model.

The resolution of the atmospheric forcing is rather coarse. Especially in Nares Strait, which is bounded by landmasses from both sides, orographic effects can have an important impact on the surface wind field. Preliminary results of FESOM-simulations with high resolution forcing data from Environment Canada (CMC GDPS Reforecast, 33 km resolution, *Smith et al.* (2013)) indicate that differences in the simulated ocean dynamics of the CAA compared to simulations with CORE-II forcing are rather small. Regarding sea ice conditions though, the high resolution forcing leads to higher sea ice transport through Nares Strait and improves the simulated ice concentration in the CAA region. An additional experiment with this high resolution forcing interpolated in time and space onto the CORE-II grid also shows improvements in the simulation of sea ice. This indicates that improvement is not just due to the resolution of the Environment Canada atmospheric forcing, but also due to its quality. The aspect of atmospheric forcing should be further investigated.

Appendix A

Vertical resolution

The vertical resolution is high in the surface layers and decreases towards the bottom (see Table A1).

Table A.1: Model z-layers with depths in m.

no.	1	2	3	4	5	6	7	8	9	10
depth	0	10	20	30	40	50	60	70	80	90
	11	12	13	14	15	16	17	18	19	20
	100	120	140	160	180	200	230	270	320	370
	21	22	23	24	25	26	27	28	29	30
	420	470	520	570	620	670	730	800	890	1000
	31	32	33	34	35	36	37	38	39	40
	1120	1260	1400	1540	1680	1820	1960	2120	2300	2500
	41	42	43	44	45	46	47	48	49	50
	2750	3000	3250	3500	3750	4000	4250	4500	4750	5000
	51	52	53	54	55					
	5250	5500	5750	6000						

Appendix B

A list of symbols

Table B.1: Symbols.

symbol	meaning
A	ice concentration
A_h	lateral momentum diffusion coefficient
A_v	vertical momentum diffusion coefficient
A_{v0}	background vertical momentum diffusion coefficient
C	tracer
C_d	bottom drag coefficient
$C_{d,ao}$	atmosphere-ocean drag coefficient
$C_{d,io}$	ice-ocean drag coefficient
$C_{e,ao}$	atmosphere-ocean transfer coefficient for the exchange of sensible heat
$C_{e,io}$	ice-ocean transfer coefficient for the exchange of sensible heat
$C_{h,ao}$	atmosphere-ocean transfer coefficients for the exchange of latent heat
$C_{h,io}$	ice-ocean transfer coefficients for the exchange of latent heat
c	empirical parameter controlling the ice strength
c_p	specific heat capacity of water

Table B.1: Symbols.

symbol	meaning
$\mathbf{F}$	internal force within the ice
F^{salt}	virtual salt fux into the ocean
F^{salt}_{P-E}	virtual salt fux into the ocean due to
	precipitation minus evaporation
F^{salt}_{ice}	virtual salt fux into the ocean due to ice melting
F^{salt}_{runoff}	virtual salt fux into the ocean due to river runoff
f	Coriolis parameter
g	gravitational acceleration
$H(x,y)$	ocean bottom depth
h	effective ice thickness
h_s	effective snow thickness
K_h	lateral diffusivity
K_v	vertical diffusivity
K_{v0}	background vertical diffusivity
$\mathbf{K}_{GM}$	Gent/McWilliams diffusion tensor
$\mathbf{K}_{redi}$	Redi diffusion tensor
L	latent heat of vaporization or sublimation
$\mathbf{k}$	vertical unit vector
m	ice mass per area
N	buoyancy frequency
$\mathbf{n}$	2D unit normal vector
$\mathbf{n}_3$	3D unit normal vector
P	ice strength
P^*	empirical parameter controlling the ice strength
p	hydrostatic pressure
Q_{LW}	long wave radiative flux
Q_{SW}	short wave radiative flux
Q_c	conductive heat flux
Q_l	turbulent flux of latent heat
Q_s	turbulent flux of sensible heat
q	surface flux
q_a	specific humidity of air

Table B.1: Symbols.

symbol	meaning
R_i	Richardson number
S	salinity
S_{ice}	salinity of sea ice
S_s	salinity of the oceanic surface layer
S_{ref}	reference salinity
S_h	sources and sinks in the ice thickness continuity equation
S_{sn}	sources and sinks in the snow thickness continuity equation
S_A	sources and sinks in the ice concentration continuity equation
T	potential temperature
T_a	air temperature
T_f	freezing point of sea water
T_s	potential temperature of the oceanic or ice surface layer
t	time
$\mathbf{u}$	horizontal ocean velocity
$\mathbf{u}_s$	horizontal ocean velocity of the surface layer
$\mathbf{u}_{10}$	horizontal wind field at 10 m height
$\mathbf{u}_{ice}$	sea ice velocity
$\mathbf{u}^*$	auxiliary horizontal velocity
$\mathbf{v}$	3D ocean velocity
w	vertical velocity
α	albedo
ϵ	emissivity
$\dot{\epsilon}$	tensor of deformation rates
η	sea surface height
λ	longitude
Φ	vertical velocity potential
ρ	mean density of sea water
ρ_0	deviation from the mean density of sea water
ρ_a	air density
ρ_i	density of sea ice
ρ_{sn}	density of snow
ρ_w	density of freshwater

Table B.1: Symbols.

symbol	meaning
σ	stress tensor
θ	latitude
τ_o	ocean surface stress
τ_{ai}	stress between atmosphere and ice
τ_{ao}	stress between atmosphere and ocean
τ_{io}	stress between ice and ocean
Ω	model domain
Γ_1, Γ_2, Γ_3	boundaries of the domain Ω
∇	2D gradient and divergence operator
∇_3	3D gradient and divergence operator
Δ	square root of the surface triangle area

Table B.2: Abbreviations.

abbreviation	meaning
AMOC	Atlantic Meridional Overturning Circulation
AO	Arctic Ocean
BIC	Baffin Island Current
CAA	Canadian Arctic Archipelago
CTD	conductivity temperature depth
DWBC	deep western boundary current
DWF	deep water formation
EGC	East Greenland Current
FEM	finite element method
FESOM	Finite Element Sea ice Ocean Model
FW	fresh water
GIN Sea	Greenland-Iceland-Norwegian Sea
LFWC	liquid freshwater content
LHW	lower halocline waters
LSW	Labrador Sea Water
MLD	mixed layer depth
NA	North Atlantic
NADW	North Atlantic Deep Water
NAO	North Atlantic Oscillation
NP	North Pacific
NWP	North West Passage
SSH	sea surface height
UHW	upper halocline waters
WGC	West Greenland Current
WSC	West Spitzbergen Current

Bibliography

Aargaard, K., and E. C. Carmack (1989), The Role of Sea Ice and Other Fresh Water in the Arctic Circulation, *J. Geophys. Res.*, *94*, 14,485–14,498.

Agnew, T., A. Lambe, and D. Long (2008), Estimating sea ice area flux across the Canadian Arctic Archipelago using enhanced AMSR-E, *J. Geophys. Res.*, *113*, doi:10.1029/2007JC004582.

Aksenov, Y., S. Bacon, A. C. Coward, and N. P. Holliday (2010), Polar outflow from the Arctic Ocean: A high resolution model study, *Journal of Marine Systems*, *83*(1-2), 14 – 37, doi:10.1016/j.jmarsys.2010.06.007.

Bailey, W. (1957), Oceanographic Features of the Canadian Archipelago, *Journal of the Fisheries Research Board of Canada*, *14*, 731–769, doi: 10.1139/f57-03.

Böning, C., M. Scheinert, Dengg, Biastoch, and A. Funk (2006), Decadal variability of subpolar gyre transport and its reverberation in the North Atlantic overturning, *Geophys. Res. Lett.*, *33*, doi:10.1029/2006GL026906.

Chelton, D. (1983), Effects of sampling errors in statistical estimation, *Deep-Sea Research*, *30*, 1083–1103.

Cheng, W., and P. Rhines (2004), Response of the overturning circulation to high-latitude fresh-water perturbations in the North Atlantic, *Climate Dynamics*, *22*, 359–372, doi:10.1007/s00382-003-0385-6.

Condron, A., P. Winsor, C. Hill, and D. Menemenlis (2009), Simulated Response of the Arctic Freshwater Budget to Extreme NAO Wind Forcing, *J. Climate*, *22*, 2422–2437, doi:10.1175/2008JCLI2626.1.

Cuny, J., P. Rhines, and R. Kwok (2005), Davis Strait volume, freshwater and heat fluxes, *Deep-Sea Res. I*, *52*, 519–542, doi:10.1016/j.dsr.2004.10.006.

Curry, B., C. M. Lee, and B. Petrie (2011), Volume, Freshwater, and Heat Fluxes through Davis Strait, 2004-05, *Journal of Physical Oceanography*, *41*, 429–436, doi:10.1175/2010JPO4536.1.

Curry, R., M. McCartney, and T. Joyce (1998), Oceanic transport of subpolar climate signals to mid-depth subtropical waters, *Nature*, *391*, 575–577, doi:10.1038/35356.

Dai, A., T. Qian, K. E. Trenberth, and J. D. Milliman (2009), Changes in Continental Freshwater Discharge from 1948 to 2004, *J. Climate*, *22*, 2773–2792, doi:10.1175/2008JCLI2592.1.

Danabasoglu, G., S. Yeager, Y.-O. Kwon, J. Tribbia, A. S. Phillips, and J. Hurrell (2012), Variability of the Atlantic Meridional Overturning Circulation in CCSM4, *J. Climate*, *25*, 5153–5172, doi:10.1175/JCLI-D-11-00463.1.

Danilov, S., G. Kivman, and J. Schröter (2004), A finite-element ocean model: principles and evaluation, *Ocean Modelling*, *6*(2), 125–150, doi:10.1016/S1463-5003(02)00063-X.

de Boyer Montégut, C., G. Madec, A. S. Fischer, A. Lazar, and D. Iudicone (2004), Mixed layer depth over the global ocean: An examination of profile data and a profile-based climatology, *J. Geophys. Res.*, *109*, doi:10.1029/2004JC002378.

de Steur, L., E. Hansen, R. Gerdes, M. Karcher, E. Fahrbach, and J. Holfort (2009), Freshwater fluxes in the East Greenland Current: A decade of observations, *Geophys. Res. Lett.*, *36*, doi:10.1029/2009GL041278.

Dickson, R., T. Osborn, J. Hurrell, J. Meincke, J. Blindheim, B. Adlandsvik, T. Vinje, G. Alekseev, and W. Maslowski (2000), The Arctic Ocean Response to the North Atlantic Oscillation, *J. Clim.*, *13*, 2671–2696.

Dickson, R., B. Rudels, S. Dye, M. Karcher, J. Meincke, and I. Yashayaev (2007), Current estimates of freshwater flux through Arctic and subarctic seas, *Progress in Oceanography*, *73*, 210–230.

Eden, C., and T. Jung (2001), North Atlantic Interdecadal Variability: Oceanic Response to the North Atlantic Oscillation, *J. Climate*, *14*, 676–691, doi:10.1175/1520-0442(2001)014¡0676:NAIVOR¿2.0.CO;2.

Fetterer, F., K. Knowles, W. Meier, and M. Savoie (2009), Sea Ice Index, Digital media, boulder, CO: National Snow and Ice Data Center.

Fissel, D., D. Lemon, and J. Birch (1982), Major Features of the Summer Near-Surface Circulation of Western Baffin Bay, 1978 and 1979, *Arctic*, *35*, 180–200.

Gent, P., and J. McWilliams (1990), Isopycnal Mixing in Ocean Circulation Models, *J. Phys. Oceanogr.*, *20*, 150–155.

Gill, A. (1982), *Atmosphere-Ocean Dynamics*, Academic Press, New York. 662 pp.

Goosse, H., T. Fichefet, and J.-M. Campin (1997), The effects of the water flow through the Canadian Archipelago in a global ice-ocean model, *Geophysical Research Letters*, *24*, 1507–1510, doi:10.1029/97GL01352.

Griffies, S. (1998), The Gent-McWilliams Skew Flux, *J. Phys. Oceanogr.*, *28*, 831–841, doi:10.1175/1520-0485(1998)028¡0831:TGMSF¿2.0.CO;2.

Hannah, C., F. Dupont, and M. Dunphy (2009), Polynyas and Tidal Currents in the Canadian Arctic Archipelago, *Arctic*, *62*, 83–95.

Hibler, W. (1979), A Dynamic Thermodynamic Sea Ice Model, *J. Phys. Oceanogr.*, *9*, 815–846.

Hibler, W. (1984), The role of sea ice dynamics in modeling CO2 increases, in *Climate Processes and Climate Sensitivity*, edited by J. E. Hansen and T. Takahashi, pp. 238–253, Geophys. Monogr. Ser., AGU, Washington D.C., doi:10.1029/GM029p0238.

Houssais, M.-N., and C. Herbaut (2011), Atmospheric forcing on the Canadian Arctic Archipelago freshwater outflow and implications for the Labrador Sea variability, *J. Geophys. Res.*, *116*, doi: 10.1029/2010JC006323.

Hunke, E., and J. Dukowicz (1997), An Elastic-Viscous-Plastic Model for Sea Ice Dynamics, *Journal of Physical Oceanography*, *27*, 1849–1867.

Hunke, E., and J. Dukowicz (2001), The Elastic-Viscous-Plastic Sea Ice Dynamics Model in General Orthogonal Curvilinear Coordinates on a Sphere-Incorporation of Metric Term, *Monthly Weather Review*, *130*, 1848–1865.

Jackett, D., and T. Mcdougall (1995), Minimal Adjustment of Hydrographic Profiles to Achieve Static Stability, *J. Atmos. Oceanic Technol.*, *12*, 381–389, doi:10.1175/1520-0426(1995)012¡0381:MAOHPT¿2.0.CO;2.

Jahn, A., B. Tremblay, L. Mysak, and R. Newton (2009), Effect of the large-scale atmospheric circulation on the variability of the Arctic Ocean freshwater export, *Clim. Dyn.*, *34*, 201–222, doi:10.1007/s00382-009-0558-z.

Jahn, A., Y. Aksenov, B. A. de Cuevas, L. de Steur, S. Häkkinen, E. Hansen, C. Herbaut, M.-N. Houssais, M. Karcher, F. Kauker, C. Lique, A. Nguyen, P. Pemberton, D. Worthen, and J. Zhang (2012), Arctic Ocean freshwater: How robust are model simulations?, *J. Geophys. Res.*, *117*, doi: 10.1029/2012JC007907.

Jakobsson, M., R. Macnab, L. Mayer, R. Anderson, M. Edwards, J. Hatzky, H.-W. Schenke, and P. Johnson (2008), An improved bathymetric portrayal of the arctic ocean: Implications for ocean modeling and geological, geophysical and oceanographic analyses, *Geophysical Research Letters*, *35*(L07602), doi:10.1029/2008GL033520.

Joyce, T., and A. Proshutinsky (2007), Greenland's Island Rule and the Arctic Ocean circulation, *Journal of Marine Research*, *65*, 639–653.

Kliem, N., and D. A. Greenberg (2003), Diagnostic Simulations of the Summer Circulation in the Canadian Arctic Archipelago, *Atmosphere-Ocean*, *41*, 273–289.

Köberle, C., and R. Gerdes (2007), Simulated Variability of the Arctic Ocean Freshwater Balance 1948-2001, *J. Phys. Oceanogr.*, *37*, 1628–1644, doi: 10.1175/JPO3063.1.

Komuro, Y., and H. Hasumi (2005), Intensification of the Atlantic Deep Circulation by the Canadian Archipelago Throughflow, *J. Phys. Oceanogr.*, *35*, 775–789.

Kuhlbrodt, T., A. Griesel, M. Montoya, A. Levermann, M. Hofmann, and S. Rahmstorf (2007), On the driving processes of the Atlantic meridional overturning circulation, *Rev. Geophys.*, *45*, doi:10.1029/2004RG000166.

Kwok, R. (2005), Variability of Nares Strait ice flux, *Geophys. Res. Lett.*, *32*, doi:10.1029/2005GL024768.

Kwok, R., and G. F. Cunningham (2008), ICESat over Arctic sea ice: Estimation of snow depth and ice thickness, *J. Geophys. Res.*, *113*, doi: 10.1029/2008JC004753.

Large, W., and S. Yeager (2004), Diurnal to decadal global forcing for ocean and sea-ice models: The data sets and flux climatologies, *Tech. rep.*, Technical Report TN-460+STR, NCAR.

Large, W., and S. Yeager (2008), The global climatology of an interannually varying air-sea flux data set, *Climate Dynamics*, *33*, 341–364, doi: 10.1007/s00382-008-0441-3.

Latif, M., C. Böning, J. Willebrand, A. Biastoch, J. Dengg, N. Keenlyside, U. Schweckendiek, and G. Madec (2006), Is the thermohaline circulation changing?, *Journal of Climate*, *19*, 4631–4637, doi:10.1175/JCLI3876.1.

Lazier, J. (1980), Oceanographic conditions at Ocean Weather Ship Bravo, *Atmosphere-Ocean*, *18*, 227–238, doi:10.1080/07055900.1980.9649089.

Lazier, J., R. Hendry, A. Clarke, I. Yashayaev, and P. Rhines (2002), Convection and restratification in the Labrador Sea, 1990-2000, *Deep-Sea Research I*, *49*, 1819–1835.

Lietaer, O., T. Fichefet, and V. Legat (2008), The effects of resolving the Canadian Arctic Archipelago in a finite element sea ice model, *Ocean Modelling*, *24*(3–4), 140 – 152, doi:10.1016/j.ocemod.2008.06.002.

Lique, C., A. M. Treguier, M. Scheinert, and T. Penduff (2009), A model-based study of ice and freshwater transport variability along both sides of Greenland, *Climate Dynamics*, *33*, 685–705, doi:10.1007/s00382-008-0510-7.

Lique, C., A. M. Treguier, B. Blanke, and N. Grima (2010), On the origins of water masses exported along both sides of Greenland: A Lagrangian model analysis, *J. Geophys. Res.*, *115*, doi:10.1029/2009JC005316.

Lohmann, K., H. Drange, and M. Bentsen (2008), Response of the North Atlantic subpolar gyre to persistent North Atlantic oscillation like forcing, *Clim. Dyn.*, *32*, 273–285, doi:10.1007/s00382-008-0467-6.

Lu, Y., S. Nudds, F. Dupont, M. Dunphy, C. Hannah, and S. Prinsenberg (2010), High-resolution Modelling of Ocean and Sea-ice Conditions in the Canadian Arctic Coastal Waters, in *Proceedings of the 20th International Offshore and Polar Engineering Conference*, beijing, China. 20-26 June 2010.

McGeehan, T., and W. Maslowski (2011), Impact of shelf-basin freshwater transport on deep convection in the western Labrador Sea, *J. Phys. Oceanogr.*, *41*, 2187–2210, doi:10.1175/JPO-D-11-01.1.

McGeehan, T., and W. Maslowski (2012), Evaluation and control mechanisms of volume and freshwater export through the Canadian Arctic Archipelago in a high-resolution pan-Arctic ice-ocean model, *J. Geophys. Res.*, *117*, doi:10.1029/2011JC007261.

Melling, H. (2000), Exchanges of freshwater through the shallow straits of the North American Arctic, in *The Freshwater Budget of the Arctic Ocean*, edited by E. L. Lewis et al., pp. 479–502, Springer, New York.

Melling, H. (2002), Sea ice of the northern Canadian Arctic Archipelago, *J. Geophys. Res.*, *107*, doi:10.1029/2001JC001102.

Melling, H., T. A. Agnew, K. K. Falkner, D. A. Greenberg, C. M. Lee, A. Münchow, B. Petrie, S. J. Prinsenberg, R. M. Samelson, and R. A. Woodgate (2008), Fresh-water fluxes via Pacific and Arctic outflows across the Canadian polar shelf, in *Arctic-Subarctic Ocean Fluxes: Defining the Role of the Northern Seas in Climate*, edited by R. R. Dickson et al., pp. 193–247, Springer.

Münchow, A., and H. Melling (2008), Ocean current observations from Nares Strait to the west of Greenland: Interannual to tidal variability and forcing, *J. Mar. Res.*, *66*, 801–833.

Myers, P., C. Donnelly, and M. Ribergaard (2009), Structure and variability of the West Greenland Current in Summer derived from 6 repeat standard sections, *Progress in Oceanography*, *80*, 93–112, doi: 10.1016/j.pocean.2008.12.003.

Myers, P. G. (2005), Impact of freshwater from the Canadian Arctic Archipelago on Labrador Sea Water formation, *Geophys. Res. Lett.*, *32*, doi:10.1029/2004GL022082.

Pacanowski, R., and S. Philander (1981), Parameterization of Vertical Mixing in Numerical Models of Tropical Oceans, *J. Geophys. Res.*, *11*, 1443–1451.

Parkinson, C., and W. Washington (1979), A Large-Scale Numerical Model of Sea Ice, *J. Geophys. Res.*, *84*, 311–337.

Peterson, I., J. Hamilton, S. Prinsenberg, and R. Pettipas (2012), Wind Forcing of Volume Transport through Lancaster Sound, *J. Geophys. Res.*, *in press.*, doi:10.1029/2012JC008140.

Prinsenberg, S., and E. Bennet (1989), Transport between Peel Sound and Barrow Strait in the Canadian Arctic, *Continental Shelf Research*, *9*, 427–444.

Prinsenberg, S., and J. Hamilton (2005), Monitoring the Volume, Freshwater and Heat Fluxes Passing through Lancaster Sound in the Canadian Arctic Archipelago, *Atmosphere-Ocean*, *43*, 1–22.

Prinsenberg, S., J. Hamilton, I. Peterson, and R. Pettipas (2009), Observing and interpreting the seasonal variability of the oceanographic fluxes passing through Lancaster Sound of the Canadian Arctic Archipelago, in *Influence of Climate Change on the Changing Arctic and Sub-Arctic Conditions*, edited by J. Nihoul, pp. 125–143, Springer.

Proshutinsky, A., R. H. Bourke, and F. A. McLaughlin (2002), The role of the Beaufort Gyre in Arctic climate variability: Seasonal to decadal climate scales, *Geophys. Res. Lett.*, *29*, doi:10.1029/2002GL015847.

Rabe, B., M. Karcher, U. Schauer, J. Toole, R. Krishfield, S. Pisarev, F. Kauker, R. Gerdes, and T. Kikuchi (2011), An assessment of Arctic Ocean freshwater content changes from the 1990s to the 2006-2008 period, *Deep-Sea Research I*, *58*, 173–185, doi:10.1016/j.dsr.2010.12.002.

Redi, M. (1982), Oceanic Isopycnal Mixing by Coordinate Rotation, *J. Phys. Oceanogr.*, *12*, 1154–1158.

Rothrock, D., and J. Zhang (2005), Arctic Ocean sea ice volume: What explains its recent depletion?, *J. Geophys. Res.*, *110*, doi: 10.1029/2004JC002282.

Schauer, U., A. Beszczynska-Moeller, W. Walczowski, E. Fahrbach, J. Piechura, and E. Hansen (2008), Variation of Measured Heat Flow Through the Fram Strait Between 1997 and 2006, in *Arctic-Subarctic Ocean Fluxes: Defining the Role of the Northern Seas in Climate*, edited by R. D. et al., pp. 65–85, Springer.

Schweckendiek, U., and J. Willebrand (2005), Mechanisms Affecting the Overturning Response in Global Warming Simulations, *Journal of Climate*, *18*, 4925–4936, doi:10.1175/JCLI3550.1.

Semtner, A. (1976), A Model for the Thermodynamic Growth of Sea Ice in Numerical Investigations of Climate, *J. Phys. Oceanogr.*, *6*, 379–389, doi:10.1175/1520-0485(1976)006¡0379:AMFTTG¿2.0.CO;2.

Serreze, M. C., A. P. Barrett, A. G. Slater, R. A. Woodgate, K. Aagaard, R. B. Lammers, M. Steele, R. Moritz, M. Meredith, and C. M. Lee (2006), The large-scale freshwater cycle of the Arctic, *J. Geophys. Res.*, *111*, doi:10.1029/2005JC003424.

Shewchuk, J. (1996), Triangle: Engineering a 2D Quality Mesh Generator and Delaunay Triangulator, first Workshop on Applied Computational Geometry (Philadelphia, PA), 124-133, ACM, May 1996.

Sidorenko, D., Q. Wang, S. Danilov, and J. Schröter (2011), FESOM under Coordinated Ocean-ice Reference Experiment forcing, *Ocean Dynamics*, *61*, 881–890, doi:10.1007/s10236-011-0406-7.

Skagseth, O., T. Furevik, R. Ingvaldsen, H. L. K. Mork, K. Orvik, and V. Ozhigin (2008), Volume and Heat Transports to the Arctic Ocean Via the Norwegian and Barents Seas, in *Arctic-Subarctic Ocean Fluxes: Defining the Role of the Northern Seas in Climate*, edited by R. R. Dickson et al., pp. 45–64, Springer.

Smith, G., F. Roy, P. Mann, F. Dupont, B. Brasnett, J.-F. Lemieux, S. Laroche, and S. Bélair (2013), A New Atmospheric Data Set for Forcing Ice-Ocean Models: Evaluation of Canadian GDPS Reforecasts, *Q. J. R. Met. S.*, submitted manusscript.

Smith, L., and S. Stephenson (2013), New Trans-Arctic shipping routes navigable by midcentury, *PNAS*, *110*, 4855–4856, doi:10.1073/iti1313110.

Steele, M., R. Morley, and W. Ermold (2001), PHC: a global ocean hydrography with a high-quality Arctic Ocean, *J. Climate*, *14*, 2079–2087, doi:10.1175/1520-0442(2001)014¡2079:PAGOHW¿2.0.CO;2.

Straneo, F. (2006), On the Connection between Dense Water Formation, Overturning, and Poleward Heat Transport in a Convective Basin, *J. Phys. Oceanogr.*, *36*, 1822–1840, doi:10.1175/JPO2932.1.

Terwisscha van Scheltinga, A., P. G. Myers, and J. D. Pietrzak (2010), A finite element sea ice model of the Canadian Arctic Archipelago, *Ocean Dynamics*, *60*(6), 1539–1558, doi:10.1007/s10236-010-0356-5.

Timmermann, R., A. Beckmann, and H. Hellmer (2002), Simulations of ice-ocean dynamics in the Weddell Sea. 1. Model configuration and validation, *J. Geophys. Res*, *107*(C33024).

Timmermann, R., S. Danilov, J. Schröter, C. Böning, D. Sidorenko, and K. Rollenhagen (2009), Ocean circulation and sea ice distribution in a finite element global sea ice-ocean model, *Ocean Modelling*, *27*(3-4), 114 – 129, doi:10.1016/j.ocemod.2008.10.009.

Wadley, M., and G. Bigg (2002), Impact of flow through the canadian archipelago and bering strait on the north atlantic and arctic circulation: An ocean modelling study, *Q.J.R. Meteorol. Soc.*, *128*, 2187–2203,, doi: 10.1256/qj.00.35.

Walker, E. (1977), *Aspects of Oceanography in the Archipelago*, Sidney, B.C.: Institute of Ocean Sciences, Patricia Bay.

Wang, Q., S. Danilov, and J. Schröter (2008), Finite element ocean circulation model based on triangular prismatic elements, with application in studying the effect of topography representation, *J. Geophys. Res.*, *113*(C05015), doi:10.1029/2007JC004482.

Wang, Q., P. Myers, X. Hu, and A. Bush (2012a), Flow constraints on pathways through the Canadian Arctic Archipelago, *Atm.-Oce.*, doi: 10.1080/07055900.2012.704348.

Wang, X., Q. Wang, D. Sidorenko, S. Danilov, J. Schröter, and T. Jung (2012b), Long term ocean simulations in FESOM: Validation and application in studying the impact of Greenland Ice Sheet melting, *Ocean Dynamics*, doi:10.1007/s10236-012-0572-2.

Wilson, K., J. Falkingham, H. Melling, and R. D. Abreu (2004), Shipping in the Canadian Arctic: Other Possible Climate Change Scenarios, in *Geoscience and Remote Sensing Symposium, 2004. IGARSS '04. Proceedings.*, vol. 3, pp. 1853–1856.

Woodgate, R. A., T. J. Weingartner, and R. Lindsay (2010), The 2007 Bering Strait oceanic heat flux and anomalous Arctic sea-ice retreat, *Geophys. Res. Lett.*, *37*(L01602), doi:10.1029/2009GL041621.

Acknowledgment